Frequency Response Modeling of Additive Friction Stir Deposition Parts with Print Defects

Brett K. Pennington

Thesis Submitted to the faculty of the Virginia Polytechnic Institute and State University in partial fulfillment of the requirements for the degree of

Master of Science

In

Mechanical Engineering

Scott T. Huxtable, Chair

Hang Z. Yu, Co-Chair

Zheng Li

May 1, 2024

Blacksburg, VA

Keywords: Additive friction stir deposition, finite element analysis, modeling, in-situ monitoring, non-destructive testing, natural frequency, frequency mode, eigenmode analysis

Frequency Response Modeling of Additive Friction Stir Deposition Parts with Print Defects

Brett K. Pennington

ABSTRACT

A change in a part's response to vibrations can be measured and utilized as a non-destructive testing method to detect deviations in the part's materials or geometry through processes such as laser acoustic resonance spectroscopy. This work focuses on leveraging vibration resonance to detect flaws in prints produced through additive friction stir deposition that arise through environmental contamination. More specifically, the use case considered is the printing of AA7075 in an iron oxide rich environment, where iron oxide dust or powder could accidentally be stirred into the printed material creating a print flaw. The modeling of printed parts contaminated with iron oxide to predict their natural frequencies is examined. Two different finite element models are discussed, which were created to represent contamination flaws with and without voids. The first model considers the case where a part is void-free. In this case, the model assumes a solid, homogeneous material condition in the stir region. The second model considers the case where voids are present in the part. This model leverages x-ray computed tomography data to build a representative mesh. These models show that with a well-understood part and corresponding flaw, it is possible to predict the natural frequencies of a flawed part. By leveraging the part vibration measurements and model predictions of known defects, it may be possible to gain insights into and characterize unknown print flaws.

Frequency Response Modeling of Additive Friction Stir Deposition Parts with Print Defects

Brett K. Pennington

GENERAL AUDIENCE ABSTRACT

An important aspect of product or part creation is checking consistency between parts. Methods that can verify a part is good without damaging the part are valuable, especially when only a few parts are being made, or there is a high chance of something going wrong. One way of checking a part is to shake it and watch how it reacts and bends. If there is a difference in how a part reacts to the shaking from a known good part, then there is a problem. This work examines creating computer simulations to predict how a part should react to shaking when it is good and how it should react when it has flaws. This work considers flaws caused by debris from the environment during part creation. This work also considers whether such debris causes holes or voids to form in the parts and conducts predictions with the holes included.

DEDICATION

I dedicate this thesis to my friends and family whose love and support has given me the strength to pursue my passions.

ACKNOWLEDGMENTS

I would like to thank my advisor Dr. Hang Yu for providing me with this opportunity to explore my interests in mechanical engineering and further my education.

I would also like to thank my colleagues and mentors: Kendall Knight and Dr. Greg Hahn. Their expertise, knowledge, and guidance through grad school have been invaluable during my time at Virginia Tech.

I would like to thank my parents, Michelle and Dirk, for their unending love, as no matter what is thrown my way, they are always in my corner.

Lastly, I would like to thank the Yu Research Group at Virginia Tech and our project collaborators at Metro Laser and the University of California, Irvine. Their hard work on sample preparation, data collection, and data processing has made this work possible.

Table of Contents

Chapter 1: Introduction

1.1 Additive Manufacturing

1.1.1 Material Control

Additive manufacturing (AM) offers many advantages over traditional manufacturing (TM) including increased part complexity, decreased material waste, and faster turn-around time [1], [2], [3], [4], [5]. However, AM processes have much less control and consistency over resulting mechanical material properties due to the high number of interacting input parameters [6]. When specifically focusing on metal AM, all the metal AM processes require either melting, sintering, or severe plastic deformation [7]. These processes significantly affect the metal's material properties or microstructure. The difficulty of AM lies in a lack of control and understanding of these processing effects. In contrast, traditional material processing procedures such as hot rolling and extrusion are well-understood and well-controlled processes that results in consistent material properties [8]. TM is also able to detect process deviations without direct material testing [9].

1.1.2 Nondestructive Testing and In-situ Monitoring

The lack of material control in AM processes creates the need for nondestructive testing (NDT) and in-situ monitoring to verify an AM part's integrity and quality [10], [11]. NDT refers to post-manufacturing testing on the finished part, whereas in-situ monitoring refers to mid-manufacturing analysis and measurements. Some examples of NDT include dye penetrant weld inspection, x-ray computed tomography, ultrasonic scanning, and vibration resonance testing. Some examples of in-situ monitoring include temperature measurement via thermocouples, thermal imaging, optical imaging, acoustic emission monitoring, and vibrational analysis. For both methods, the part and its material remain unimpacted from testing or inspection, but data must be correlated to properties of interest. This contrasts with many traditional material testing methods, such as tensile, fatigue, and hardness testing, all of which break or leave marks on the part. These traditional methods provide direct data on the desired material properties or part performance at the cost of sacrificing a part. With consistency and confidence in the manufacturing process, this destructive method of testing is acceptable, as a test specimen can represent a batch of parts. However, as outlined above, metal AM methods do not have this consistency. Therefore, an NDT or in-situ monitoring method that can be directly connected to the material properties of an individual AM part would be invaluable to any AM process.

1.2 Additive Friction Stir Deposition

1.2.1 Background and Advantages

Additive friction stir deposition (AFSD) is a novel additive manufacturing (AM) technique that applies the friction stir principle to deposit solid metal. The deposited metal undergoes intense heating and large strains and strain rates during deposition; however, the metal does not melt[12], [13], [14]. The feed material is a square cross-section rod that deforms into a thin, wide track as it is forced out of a spinning toolhead as illustrated in Figure 1. The spinning toolhead provides an energy input mechanism to generate frictional and viscous heating and apply the mechanical work necessary to plastically deform the feed material. A print also requires a substrate to deposit the feed material onto. The substrate should be compatible with the feed material, as this promotes the metallurgical bonding of the stir.

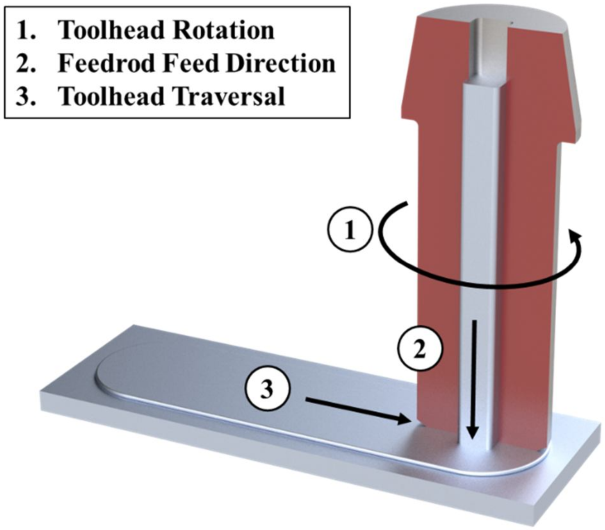

Figure 1: AFSD track render with a cutaway tool

Compared to other metal AM techniques such as wire arc AM or laser power bed fusion, AFSD stands out in its non-melt, solid-state operation. AFSD also can produce fully dense depositions of wrought-strength material [15], [16]. Due to these advantages, AFSD is being targeted as a solution to structural modification and part repair [17], [18], [19]. These and other areas of interest lead to the desire to employ AFSD in austere environments outside of the ideal manufacturing and lab environments that the process is typically operated in.

1.2.2 Use in an Austere Environment

The target use case of AFSD for part modification and repairs leads to in-field use. This brings the AFSD machine out of an ideal manufacturing environment free of contamination and into one where contamination and non-ideal surroundings must be handled. One of the main concerns of printing in an austere environment lies in printing defects that arise from the environment itself. For example, foreign debris such as dirt or dust could blow into the printer and become embedded in the deposition. This and other potential print flaws add another complication to controlling AFSD. In situ detection and automatic mitigation of print flaws due to such conditions would enable the use of AFSD in austere environments despite the added complexity and risks.

This paper considers printing in an iron oxide ($Fe2O3$) rich environment, such as on the surface of Mars, with the premise that iron oxide dust could land on the print and be stirred into the printed material. Iron oxide is considered a contaminant in the print and therefore would need a method of in-situ detection. Vibration resonance was chosen as the method of NDT detection for iron oxide contamination in this study. The overarching study aims to develop a method of in-situ monitoring that can detect contamination mid-print through part resonance and determine the impact of the iron oxide contamination on the printed material's mechanical properties.

1.3 Laser Acoustic Resonance Spectroscopy

1.3.1 Vibration Fundamentals

When an object or system experiences cyclical impulses or vibrations, the system will deform in an oscillatory manner. The rate at which the impulses occur is referred to as the frequency, measured in cycles per second or Hertz (Hz). Every non-rigid object or system has specific frequencies known as natural or modal frequencies that will result in heightened deformation amplitudes during vibration. The shape in which the object deforms when subjected to impulses at one of these modal frequencies is known as a mode shape. This shape is dynamic as the object oscillates between zero deformation from its at-rest state to the deformed mode shape at the modal frequency. The oscillatory deformation of an object is comparable to a standing wave where some sections of the object can experience zero deformation while other areas experience a high deformation amplitude. The areas where there is zero deformation are referred to as nodes and the areas of highest deformation are referred to as antinodes. An object's natural frequencies are a product of its material and geometry [20]. So, due to the theoretically infinite number of natural frequencies for every object, an object's natural frequencies are unique to it [21]. Therefore, if an object's natural frequencies change, it can be deduced that its geometry or material also changed. It is also important to note that boundary conditions will affect a system's resonance response as well. For example, if a part is fixed at one end, this not only changes the deformation shapes but also the natural frequency values.

Looking at a fundamental vibrations problem as seen in Figure 2, an undamped mass oscillating on a spring has the natural frequency (ω_0) that is defined by the spring stiffness (k) and mass (m) as defined in Equation 1. Although this equation cannot be directly applied to 3D objects and more complex systems, it shows the fundamental relationship between an object's material properties, geometry, and natural frequencies. In this relationship, the stiffness of an object is related to its elastic modulus and geometry, and the mass of an object is defined directly by its size and density.

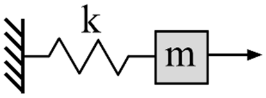

Figure 2: Fundamental mass-spring vibration diagram

$$\omega_0 = \sqrt{\frac{k}{m}} \tag{1}$$

When an object experiences a natural frequency, the mode shape it deforms into is unique for that frequency. That is, each natural frequency has a unique mode shape attached to it. For this case study, an ASTM E8 sub-size tensile bar was used as the geometry for all the samples. For the tensile bar, four fundamental mode shapes need to be considered: out-of-plane bending modes, in-plane bending modes, twisting modes, and elongation modes. For the in and out of plane modes, the reference plane lies parallel to the wide flat face of the tensile bar with the gauge section features on its cross-section. With this reference plane, the out-of-plane bending modes include deformation away from the reference plane. The in-plane bending modes do not break the reference plane as the deformation lies within the plane. The twisting modes show a rotational deformation along the length of the bar, and the elongation modes occur due to stretching or compression along the length of the bar. An example illustration of each of these fundamental mode shapes is shown in Figure 3. Beyond these shapes, others are possible, such as combination modes which exhibit deformation of two or more of these types of mode shapes in one mode.

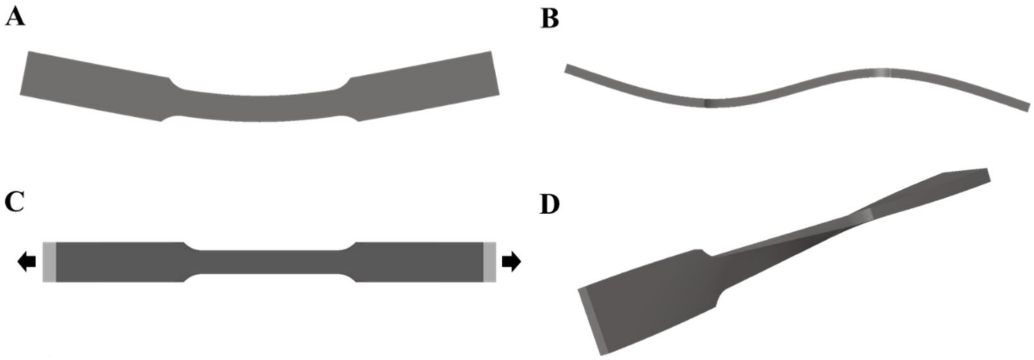

Figure 3: Mode shape deformation example plots: (A) In-plane bending, (B) Out-of-plane bending, (C) Elongation, (D) Twisting

As the natural frequency value increases, the number of deformation peaks also increases. For example, the lowest natural frequency of the tensile bar corresponds to an out of plane bending mode with a single deformation peak. While deformed this shape looks like a “U”. The next out-of-plane bending mode shape exhibits two deformation peaks and looks like an “S”. This pattern continues onto the third out-of-plane bending mode with three peaks and so on as illustrated in Figure 4. These modes and their corresponding frequency value will be named after their bending mode shape and a number that relates to the number of peaks the shape exhibits, such as out-of-plane bending mode 3. The order of appearance of the mode shapes is not necessarily cyclic. For example, several out-of-plane bending modes appear before a twist or elongation mode shows up in order of increasing frequency on the tensile bar.

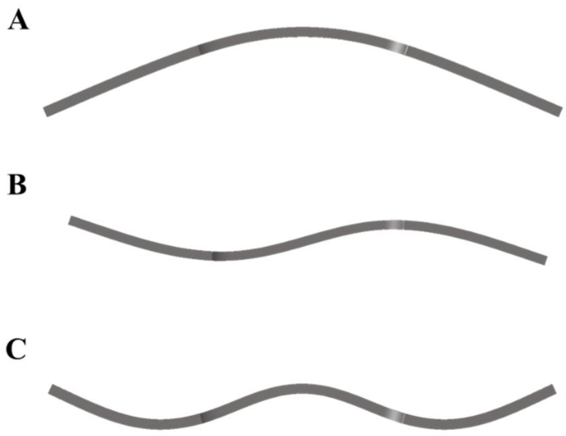

Figure 4: Out-of-plane bending mode shapes of increasing frequency: (A) First out of plane bending mode, (B) Second out of plane bending mode, (C) Third out of plane bending mode

1.3.2 Excitation and Measurement

Laser acoustic resonance spectroscopy (LARS) is an NDT method based on measuring a part's vibration resonance spectrum. The peaks of the measured spectrum indicate the part's natural frequencies. These natural frequencies can be used to identify a part due to its unique frequency spread. This also allows LARS to detect changes from a baseline part that result from geometric or material differences. To measure a part's vibration spectrum, the part is excited with a sweep of vibration frequencies applied at a point by a piezo-electric transducer. This sweep is a linear sweep across frequencies from ~10kHz to ~40kHz. During measurement, the velocity of a single point on the part is recorded throughout the sweep by a laser Doppler vibrometer. Due to the presence of nodes, the measurement is repeated several times looking at different points on the part to ensure that many vibrational modes are detected. It is important to note that without using multiple setup orientations, LARS will not pick up every vibration mode, as the vibrometer can only detect deformation in a single direction normal to its measurement direction. The combined velocity across the different measurements gives an overall vibration resonance spectrum for the entire part reported as a velocity versus frequency graph curve [22], [23], [24], [25].

1.3.3 Experimental Setups

As explained above, LARS measurement requires part excitation, part holding, and a response measuring device. Metro Laser (Irvine, CA) conducted LARS measurement for this case study and used two different experimental setups throughout the study. Improvements were made to their setup between the two batches of samples, so the same setup was not used for the duration of the study. The difference between these two setups lies in the part holding, as both setups use the same equipment for part excitation and vibration measurement. For part excitation, a piezoelectric actuator (piezo) that the part rests on was used. The piezo was clamped to rigid rods to hold it in place. A laser vibrometer, which was connected to a Galvo scanner, was mounted above the part. This vibrometer measured the part's response during the excitation sweep from the piezo. The Galvo mirror allowed for precise control of the measurement location on the part without having to adjust the piezo or part itself. The vibrometer required a non-reflective surface for accurate measurements, so white tape was applied to the part over the measurement spot and the tape was assumed to have a negligible effect on the measurement.

Both experimental setups aimed to approximate a free boundary condition, as a free boundary condition would equate to unrestricted and undamped vibration of the part. The first experimental setup used a 45-degree ramp to support the part. Renderings of this setup can be seen in Figure 5. The piezo sat at the bottom of the ramp to create a v-like hold for the bottom of the part. This supported one end of the part. The other end of the part sat in a parallel v-hold next to the ramp. To minimize friction and damping, the main ramp had a sheet of Teflon (PTFE) as the only material in contact with the part. For rigidity, this Teflon sheet was backed by a metal plate. Renderings of their second experimental setup can also be seen in Figure 5. This setup used a fabric net to support the part during excitation. The net was held in place by 4 pillars at the net’s four corners. The piezo sat underneath the net and poked through it to contact the part and perform excitation.

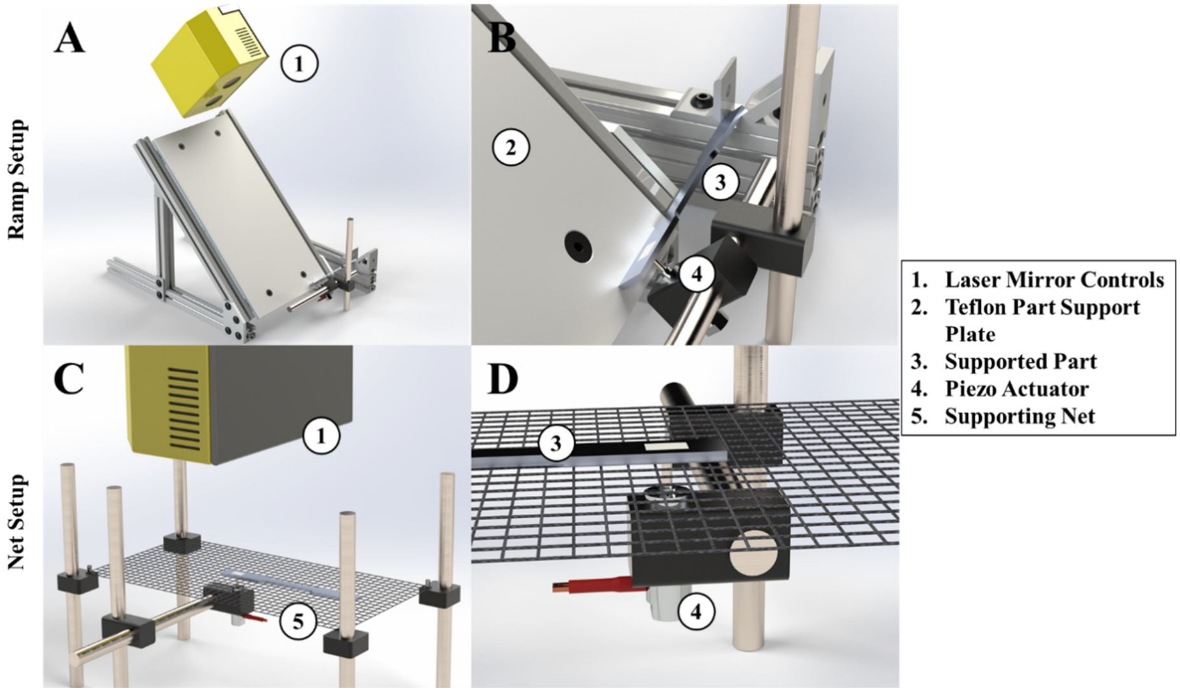

Figure 5: LARS experimental setup CAD renders: (A) Ramp setup overview, (B) Ramp setup closeup, (B) Net setup overview, (C) Net setup closeup

1.4 Finite Element Analysis

1.4.1 Background

Finite element analysis (FEA) was used to build models for simulating a sample's resonance spectrum and material properties. FEA is a method of numerical analysis that can be used to evaluate arbitrary systems for many types of engineering problems including mechanics, vibrations, and heat. Compared to a direct equation-based solution, FEA has the advantage of being able to consider arbitrary geometries and loading conditions without the need for gross simplifying assumptions. This is done by splitting the system into discrete sections or elements. The resulting combination of all the elements is referred to as a mesh. This division is the basis of the finite element method. For three-dimensional problems, these elements are generally tetrahedrons or hexahedrons and are connected at their corners or nodes. The two-dimensional equivalents are triangular and quadrilateral elements respectively. Of these element geometries, hexahedrons or quadrilateral elements are generally preferred due to their faster solution convergence and higher meshing efficiency [26].

A meshing strategy that a modeler can implement to create a better or more intricate mesh is partitioning. Simply put, partitioning is the splitting of the model geometry into sections. The utility of having discrete geometric sections is multifaceted. For meshing, partitioning can allow for more complicated geometries to mesh with the more desirable hexahedral or quadrilateral elements. Partitioning can also create more control for element sizing and distribution or allow different types of elements to be used in different sections of the geometry. Beyond meshing advantages, partitioning allows different material properties to be applied to different sections of a single body.

In addition to a mesh, an FEA model requires boundary conditions (BCs) and loads. For static simulations, boundary conditions can include fixed geometric features, prescribed displacements, or symmetry. Loads are like boundary conditions but involve prescribing forces or pressures to geometric features. Loads and boundary conditions can also include thermal, electrical, and other types of inputs depending on the simulation.

1.4.2 Eigenmode Analysis

As explained in section 1.3, LARS is a method to measure a part's natural frequencies. The equivalent FEA modeling technique is eigenmode analysis. Eigenmode analysis simulates vibrating a part and solves an eigenvalue problem to determine what vibration frequencies cause peak deformation shapes to occur. The software creates a mass and stiffness matrix from the mesh. From these, the software can solve for the natural frequencies and corresponding mode shapes through an eigenvalue solution algorithm [27]. The exact algorithm and solution vary with different solvers and software packages. Since eigenmode analysis is an FEA technique, it uses a representative mesh of the part it simulates. Compared to a physical object, which has infinite degrees of freedom for deformation and displacement, a mesh has a finite number of degrees of freedom based on the number of nodes in the mesh. Eigenmode analysis assumes the mesh has enough nodes to represent the deformation mode shapes of the physical part. As outlined above, higher frequency mode shapes become more complex, so this assumption becomes worse with higher frequencies. It is important to note that the predicted deformation magnitude from eigenmode analysis is arbitrary without providing excitation and damping magnitudes. The eigenmode analysis conducted in this case study also assumes that the material behaves as linearly elastic. The eigenmode models were run unconstrained, without BCs. This is an idealization of the BCs and represents if the part were floating in a vacuum. The LARS setup aims to approximate this environment, so the atmospheric air around the part and the part holding ramp or net were assumed to be negligible.

Due to its single-point measurement, LARS only detects modes in a single deformation direction and is unable to estimate mode shapes. In contrast, the eigenmode analysis estimates all the part’s natural frequency modes and deformation shapes within the specified frequency range. So, the eigenmode predicted mode shape needs to see deformation in the LARS vibrometer measurement direction to expect a comparable frequency in the LARS data.

Chapter 2: Multi-Scale Tensile Bar Model

2.1 AFSD Printing with Contaminants and Machining Tensile Specimens

The need to print in austere environments necessitates the development of NDT techniques that can detect foreign matter in an AM deposition. To study this more closely, iron oxide (Fe_2O_3) was taken as a potential contaminant in an AA7075 deposition. To study the effect of contamination on material properties and NDT evaluation methods, ASTM E8 tensile bars were manufactured that contained varying levels of iron oxide. The manufacturing method, which is outside the scope of this work, see [17], was copied over from earlier work on repairing holes in 7xxx series aluminum using AFSD.

The AA7075 substrate for the hole-repair prints had a 0.25in diameter hole machined halfway through its 0.25in thickness. The desired amount of Fe_2O_3 powder for each print was then measured on a mass scale and carefully poured into the substrate's hole as illustrated in Figure 6. As is standard with a hole repair print, a pinned tool was used. This means that the bottom of the tool face had small protrusions rather than being a smooth, flat surface. During printing, the pins on the tool head engaged with the substrate material, and helped to break down the hole feature, and provided more mixing during the deposition. After the pins began stirring the substrate, the feed rod was advanced to begin flowing material into and filling the hole. Then the toolhead lifted slightly and more feed material was fed into the stir. This process was repeated three times until the tool and its pins were above the substrate surface to allow for a flush top once machined.

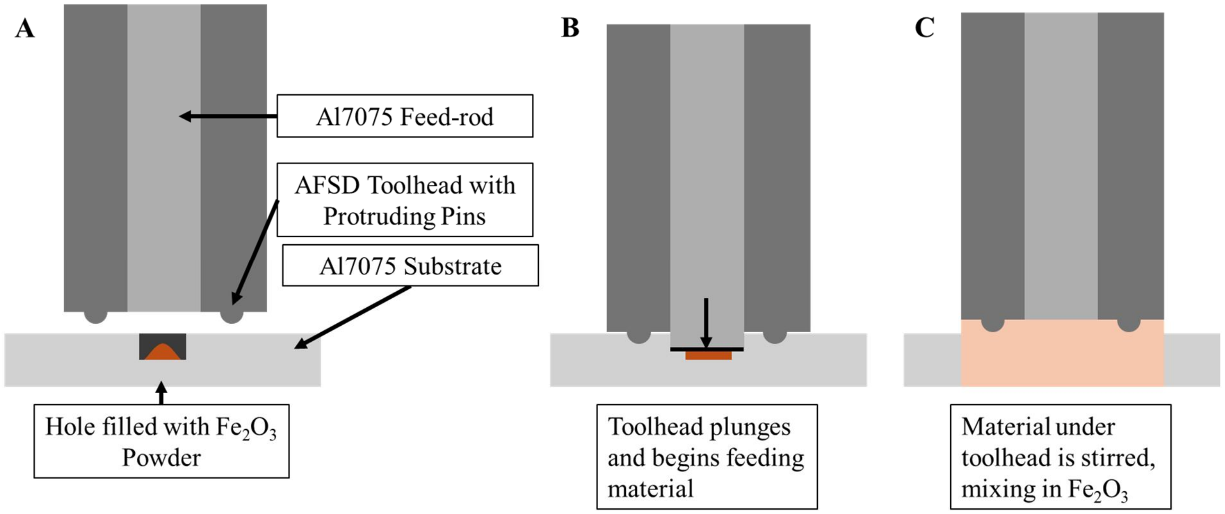

Figure 6: Hole repair print process diagram: (A) Pre-print preparation stage, (B) Start of hole repair print, (C) End of hole repair

For the first batch of tensile bar samples, 9 hole-repair coupons with varying amounts of Fe_2O_3 in the hole were printed. Three samples each of 0.00g, 0.03g, and 0.06g of Fe_2O_3 were produced. These were printed under ideal processing conditions and resulted in solid, porosity-free depositions. One of the 0.06g samples was rendered unusable during the study and is left out of consideration for any analysis or results which leaves 8 printed samples. Among these samples, the 0.00g samples did not include any iron oxide in the print to serve as a baseline AFSD part without any contamination or intentional flaws. These samples were printed first to avoid iron oxide cross-contamination and were printed and stirred purely with AA7075.

For this study, rather than re-machining the hole feature in the substrates as is typical with a hole repair print, the prints were machined into ASTM E8 subsize tensile bars. This geometry allowed for tensile testing on the specimens and is discussed in section 2.3 in further detail. The post-print machining process began with water jetting the tensile bar shape out of the substrate as illustrated in Figure 7. This process was outsourced to a machine shop. The water jet only cut the outline of the tensile bars and did not cut the specimens to the correct thickness. So, once the samples came back from the machine shop, they were milled to thickness to finalize their dimensions.

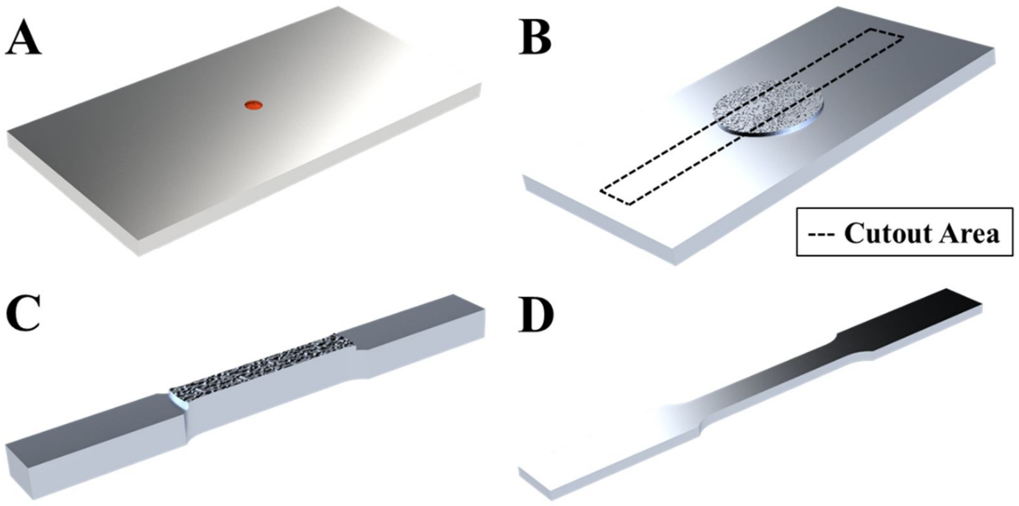

Figure 7: Tensile bar sample manufacturing steps: (A) AA7075 substrate with Fe2O3 before printing, (B) Resulting geometry after AFSD printing with excess material above substrate surface, (C) Water jet tensile bar cutout, (D) Final polished tensile bar geometry

It is important to note that the amount of iron oxide should be treated as a label rather than a precise measurement. As explained above, the iron oxide amount is carefully measured and placed in the substrate hole before printing, but this amount is not retained in the final tensile bar for several reasons. First, during printing, the spinning of the toolhead results in some of the iron oxide flying out of the hole, and this uncontrolled amount is not stirred into the print. Also, the entire print volume is not retained in the final tensile bar geometry as much of it is machined or cut away. This is illustrated clearly with a 2D representation in Figure 8 where the dashed red circle shows a projection of the stir and the missing volume outside the tensile bar area. A similar print region volume loss occurs when machining the top and bottom of the tensile bar to bring it to the ASTM designated thickness.

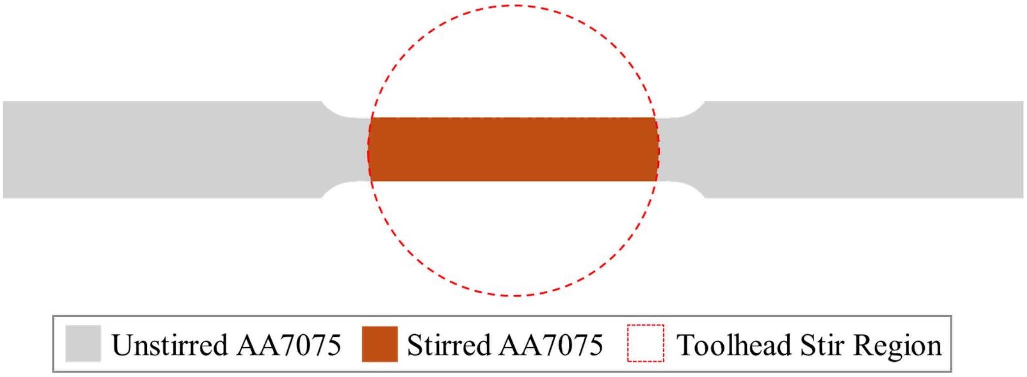

Figure 8: Print stir region overlayed onto tensile bar geometry

2.2 LARS Measurement Results

After the samples were machined, they were sent to Metro Laser to have their vibration spectra measured via LARS. The first batch of samples used the ramp setup shown in Figure 5. The samples were scanned from a range of 10 to 40kHz. Vibration measurements were also only taken normal to the wide face of the tensile bar, so only modes that deform out of plane in this direction were detected. Relative to mode shapes, this means that LARS is generally only reading out-of-plane bending modes and twisting modes. The combination of these two limitations inherently limited the natural frequencies available for analysis. The vibrometer velocity measurements were plotted against frequency in Figure 9. Here, four vibration spectra were plotted, which correspond to each of the iron oxide amounts in the first batch (0.00g, 0.03g, and 0.06g). For each plot, only one sample's frequency response within each iron oxide amount grouping was plotted for clarity. From these plots, the natural frequencies of each sample were extracted, as the velocity peaks indicated a natural frequency. Across the samples, there was a relative consistency in the spectra regarding the number, amplitude, and frequency location of the peaks. So, discerning the differences between these samples was a matter of individual frequency shifts rather than holistic spectra change. This outcome was expected due to the consistency in the geometry of the samples.

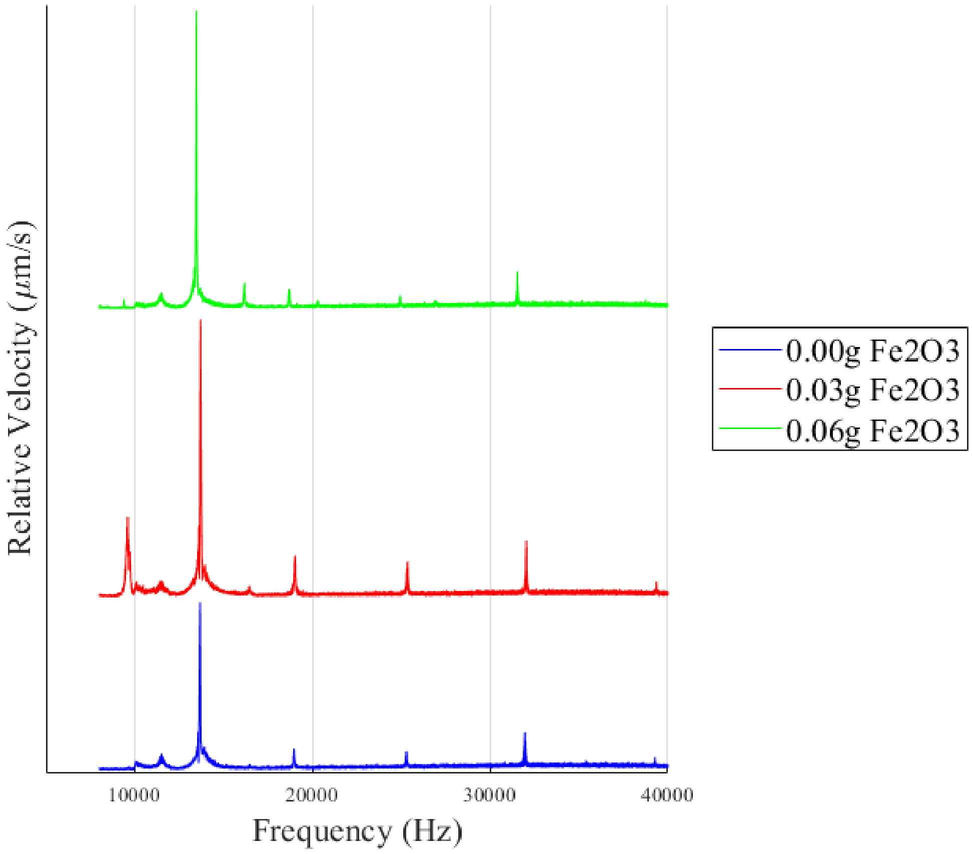

Figure 9: Batch 1 samples LARS frequency plots

Due to the relatively small shift percentages of the natural frequencies between samples, it was difficult to illustrate these shifts from the LARS frequency plots. It was easier to analyze trends by extracting the natural frequency values at the vibration spectrum peaks across all the samples. The consistency between each spectra allowed four of the peaks to be tracked across the samples. Illustrated in Figure 10 are plots of the natural frequencies against the initial iron oxide amount in each sample. Here, the 0.0g iron oxide samples were considered a baseline. The natural frequencies in each iron oxide group were also averaged and plotted. Across all the plots, the natural frequencies decreased with more iron oxide added to the print. From the fundamental frequency equation, this trend indicated either a decrease in part stiffness or an increase in the density of the printed region. Iron oxide is denser than aluminum, so it would make sense that adding a significant amount of iron oxide would increase the density of the printed region and lead to a frequency shift. However, the maximum amount of iron oxide added to any print in this group was 0.06g of iron oxide, and not all the iron oxide was retained in the final tensile bar. The low initial amount combined with lost iron oxide through machining meant any change in bulk part density was negligible. The stiffness of the part could have changed with geometric or elastic modulus changes. However, the geometry of the first batch of samples was held to tight tolerances and no geometric correlation was found. This left the elastic modulus as the sole explanatory variable for the trend in peak shifts. Iron oxide has a higher elastic modulus than aluminum, so through composite theory, an increase in the elastic modulus would be expected from the addition of iron oxide [28]. However, it was predicted there was a lack of metallurgical bonding between the iron oxide and aluminum. This non-rigid bond would explain a decrease in the elastic modulus and explain the natural frequency shifts.

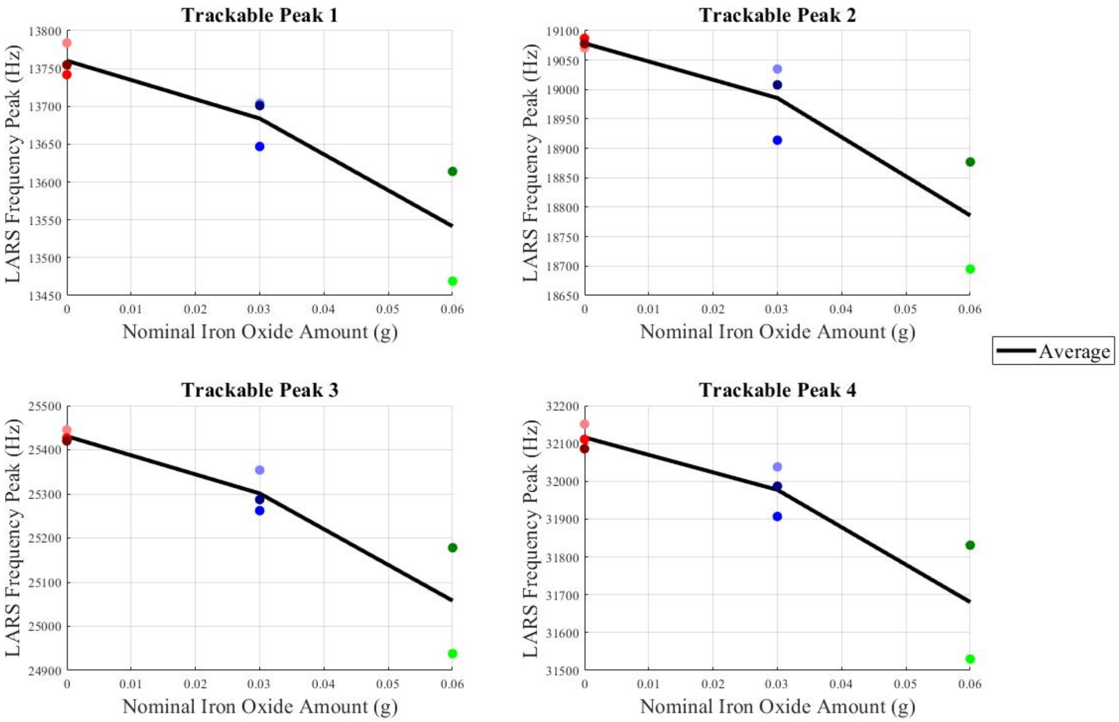

Figure 10: Natural frequency shift plots for each trackable peak from the batch 1 sample group

These trends were not as well defined as was anticipated when planning the experiments. There is a relatively large variation within each group of samples based on the initial iron oxide amount. This could partially be explained by the inconsistency or lack of control for how much of the iron oxide ended up in the final specimens. The trends illustrated in Figure 10 were based on the initial iron oxide amounts and therefore the assumption that this initial amount is a relative indicator for the final iron oxide amount to group the samples accordingly. So, when looking to model the frequency response of these tensile bars, more insight into the iron oxide distribution was needed, which led to the use of SEM imaging.

2.3 Scanning Electron Microscope (SEM) Imaging

In this case study, SEM served as another NDT method for collecting data and insight into how the tensile bar specimens were affected by the iron oxide. Relative to modeling, SEM provided a way to visualize the distribution of retained iron oxide within the samples. The highest iron oxide samples (0.06g) showed high-concentration streaks of iron oxide as shown in Figure 11. However, the lower iron oxide samples (0.03g) did not have these streaks and only showed well-distributed lighter spots also shown in Figure 11. These spots were verified to be iron oxide through EDS scans as shown in Figure 12. There was higher iron and oxygen content detected in white regions (part 3) compared to darker regions (high count dark area). With the white regions taken to be iron oxide and the gray regions taken to be AA7075, SEM can be used to inform the distribution and amount of iron oxide in different regions of the tensile bar.

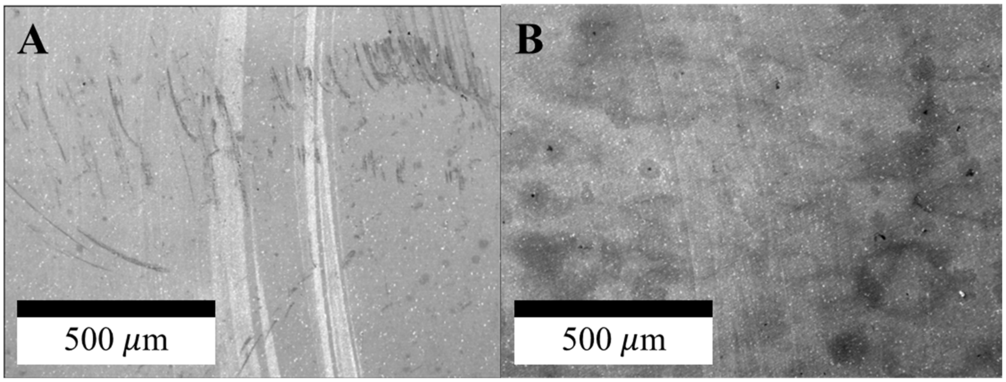

Figure 11: (A) SEM image of 0.06g sample with iron oxide streaks, (B) SEM image of 0.03g sample with well-distributed iron oxide

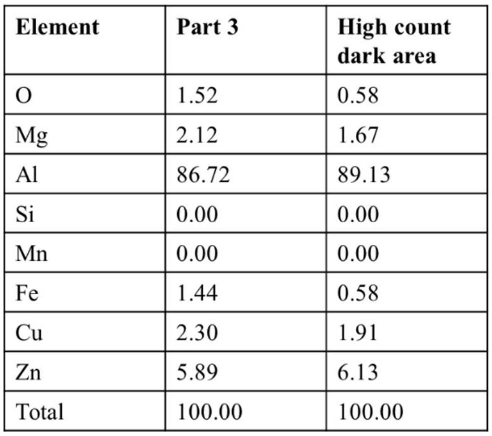

Element	Part 3	High count dark area
O	1.52	0.58
Mg	2.12	1.67
Al	86.72	89.13
Si	0.00	0.00
Mn	0.00	0.00
Fe	1.44	0.58
Cu	2.30	1.91
Zn	5.89	6.13
Total	100.00	100.00

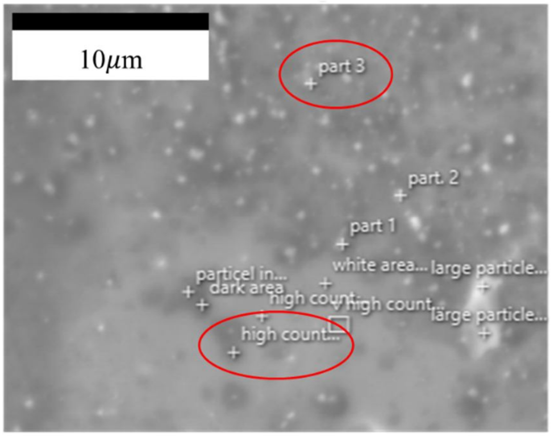

Figure 12: SEM imaging EDS scan results for light and dark regions of image

2.4 Tensile Testing Results

With the LARS frequency measurements complete, tensile testing was conducted on the samples. The tensile tests were conducted on an Instron 4468, an ultimate tensile testing machine (UTM) machine with a 50 kN load cell. The data collected included stress and strain from the extensometer. Plotted in Figure 13 is an example stress-strain curve from the tensile bar samples. From the stress-strain curves, the elastic modulus of each sample was calculated as the slope of the linear elastic portion of each plot. The elastic modulus for each sample is shown in Table 1. As shown in Figure 13, the calculated modulus of elasticity for each sample is plotted against the nominal iron oxide amount. This plot shows that there is not a clear trend between the iron oxide amount and the modulus of elasticity. However, there is also a significant amount of variation between samples in the same iron oxide group. So, the data does not clearly show that the modulus is constant either. As explained in Section 2.2, the elastic modulus was expected to decrease with an increase in the iron oxide to explain the frequency shifts. However, this expected trend is neither supported nor refuted by the tensile data. So, the average of all the points was used as a baseline elastic modulus for the stir region rather than trying to use individual points.

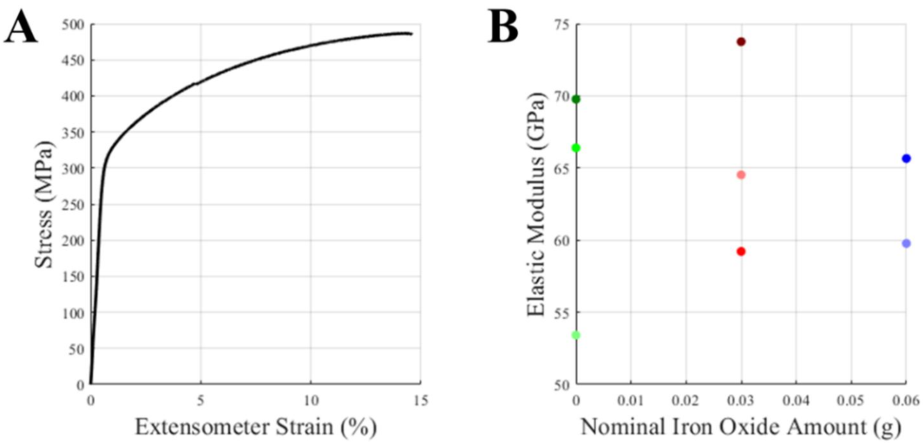

Figure 13: (A) Example stress-strain curve from sample 1, (B) Elastic modulus vs nominal iron oxide amount distribution

Sample #	Nominal Fe2O3 (g)	Elastic Modulus (MPa)
1	0	53.4
2	0	66.4
3	0	69.8
4	0.03	64.5
5	0.03	59.2
6	0.03	73.8
7	0.06	59.8
8	0.06	65.7
	Average:	64.1

Table 1: Stir region elastic modulus table

2.5 Multi-Scale Model Overview

Modeling of the first batch of samples began with their SEM images and LARS signal data. The goal of the model was to correlate changes or shifts in the LARS vibration spectrum to changes in stir region elastic modulus due to the presence of iron oxide. The model assumed that the tensile bar could be treated as a two-material solid where the center stir has a set of material properties and the rest of the tensile bar, mostly consisting of the grips, had independent material properties. For the grip sections, the material properties were assumed to be the material properties for AA7075 T6 with a density of 2.81g/cm^3 and an elastic modulus of 72GPa [29]. The model assumed that the stir region was homogenous or uniform in its material properties or could be approximated as such. While modeling these samples, the stir region elastic modulus was tuned based on the frequency shifts. However, to simulate unknown print defects, the model also needed to predict the stir region material properties based on a nominal iron oxide amount.

However, the microscopic size of the iron oxide powder particles created a problem for direct simulation within the model.

With systems that involve intricate geometry or features that exist at different orders of magnitude, creating a model with a mesh that can solve with a reasonable computation time can become impossible. For example, including many fasteners with threads in a large assembly vastly increases the required number of elements required to mesh a design. For the iron oxide and tensile bar composite model, the SEM showed that the iron oxide particles were several orders of magnitude smaller than the tensile bar itself. Attempting to include individual particles in a full-scale tensile bar geometry would have resulted in a very large number of elements in the mesh on the order of around 10^15 and a correspondingly high computation cost. For reference, an element count on the order of 10^6 was the reasonable limit for this model and the computers available. To overcome this computational challenge, a multi-stage model bridged the gap between the physical orders of magnitude to consider the microscale effects of the iron oxide in a macroscale tensile bar model. The model consisted of multiple geometric scale levels. Each model scale fed its results into the next. This meant that several order of magnitude scales of material effects could be considered in a single combined model without an unnecessary number of elements.

The goal of the multi-scale model was to simulate the aluminum and iron oxide mixture in the tensile bar on multiple scales to capture all the physical effects. The model was informed by SEM images and the goal was to calibrate the model using the LARS data so that unknown flaws could be simulated. The SEM images provided the iron oxide particle shape, size, and distribution for each sample. The modeling platform included three individual FEA models on different scales hereafter referred to as the microscale, mesoscale, and macroscale. The micro and mesoscale models aimed to estimate the material properties of each sample using the SEM images. The need for two models to estimate the material properties lies in the geometric complexity of the mixtures. The microscale model considered individual iron oxide particles and their effect on the bulk material elasticity, while the mesoscale used the microscale results to estimate the material properties over the stir region while taking iron oxide concentration gradients into account. The largest scale, the macroscale, was a full tensile bar eigenfrequency model that estimated the natural frequency modes.

2.6 Multi-Scale Model Scales

The microscale and mesoscale models were created with a 2D simplification. This 2D assumption was made to simplify the model on the basis that these models were only being used to estimate material properties, so 3D geometry does not add to the model. The microscale model aimed to simulate the effects of individual iron oxide particles stirred into the AA7075 as a composite material. The model assumes linear elastic behavior from its components. The model is informed by two SEM images as its inputs as shown in Figure 14. The microscale model was bound within a 5um square section, the same size as the SEM input image, and the iron oxide particles were approximated as circles, as they appeared relatively round in the SEM image. The image also showed that the particles are not uniform in size. From this image, a size range for the iron oxide particles was used to inform the microscale model's geometry generation as shown in

Figure 15. The size range of the particles appeared consistent across all the samples, so this range was held constant in the model. The model based the number of particle circles to generate on an area fraction input. This area fraction was calculated from a subsection of the mesoscale SEM image also seen in Figure 14. The model generated circles, randomized in size and position, within the square section until the specified area fraction of iron oxide was met. The iron oxide particles were also not allowed to intersect each other or the square section boundaries during generation. These restrictions were necessary for the partitioning and auto-meshing procedure. The generation stochastically represented the iron oxide distribution within the tensile bars using only the area fraction and size bounds as input parameters.

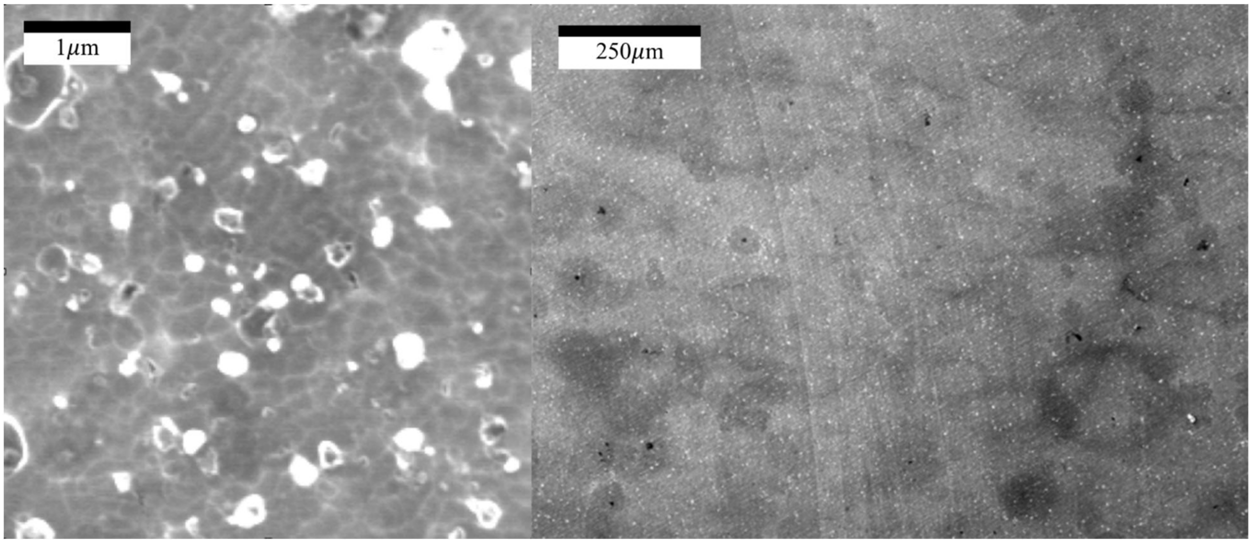

Figure 14: SEM images to inform microscale and mesoscale models

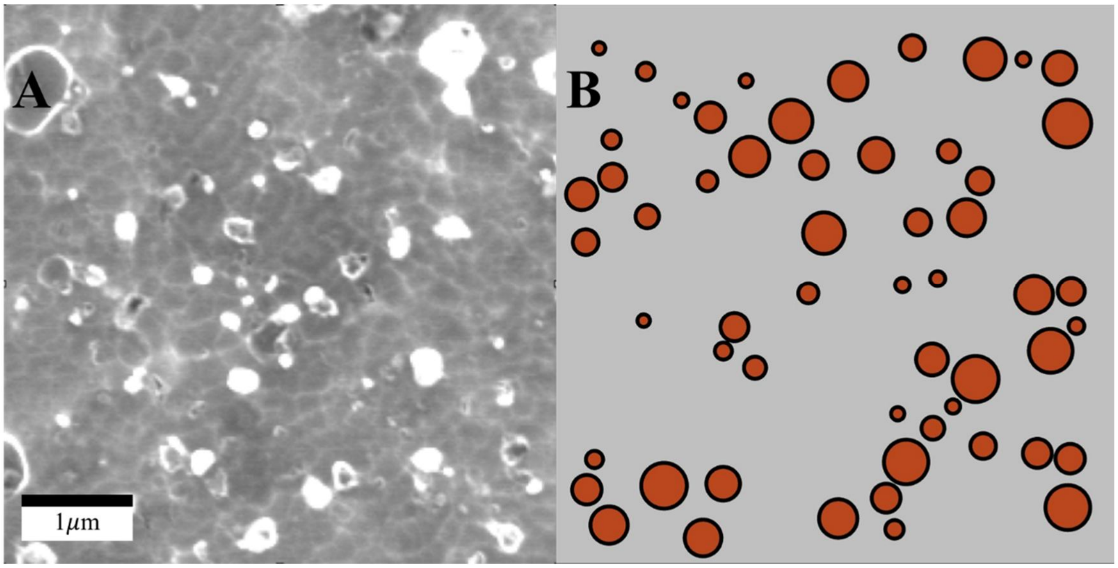

Figure 15: (A) Microscale SEM image, (B) Microscale stochastic model generated geometry

The inclusion of randomized geometry in the microscale model was necessary to create a flexible model that could consider an arbitrary iron oxide area fraction. The immediate concern was the variability of the model output simply due to the differences in the randomized geometry. To test this, the microscale model was run 50 times with the same inputs and parameters. This meant that the area fraction of iron oxide, iron oxide particle size range, material properties, and model assumptions were constants for all 50 runs. The only variable was the randomized distribution of the iron oxide particles within the section and their radius within the constant size range. As seen in Figure 16, these runs resulted in a range of around 1GPa for the output modulus with what appears to be a normal distribution. The model shows stability through this distribution.

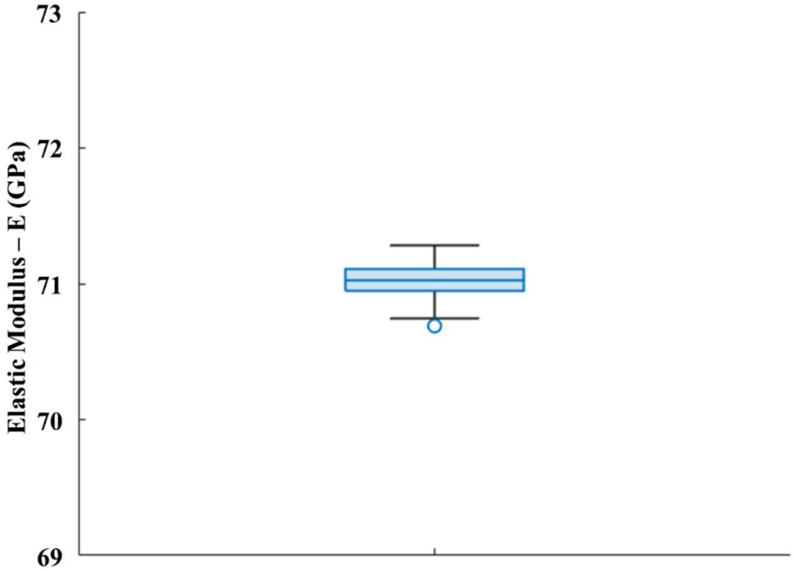

Figure 16: Stochastic geometry effect on elastic modulus output of microscale model

Based on the trends from the LARS data in Section 2.2, a higher amount of iron oxide correlated to a decrease in the natural frequency values. This negative shift indicated a decrease in the stiffness of the part and therefore a decrease in the stir region elasticity. From composite theory and the rule of mixtures, the overall strength of the aluminum composite would be expected to increase due to the higher strength of the iron oxide [28]. To account for the elasticity decrease, the microscale model also included a small shell feature around each iron oxide particle. The shells were built into the model as circles centered on each iron oxide circle. The shells were slightly larger than the iron oxide such that there was a constant difference in radii or thickness to all the shells. The shell represented the bond interface between the aluminum and the iron oxide particles. Since there was no metallurgical bonding between them, the shell was expected to have a lower elastic modulus than both the iron oxide and the aluminum. The modulus of elasticity of the shells was therefore unknown and was designated as the tuning parameter for the model to match the material properties and LARS frequency shifts. The microscale model was run several times with constant inputs except for a variable elastic modulus in the shell. This was done to observe the shell's effect on the overall material elastic modulus. As illustrated by the results of these runs in Figure 17, the weak bond interfaces approximated by the shell geometry effectively negated the strengthening effect of the iron oxide when the shell has a relatively low elastic modulus compared to the aluminum.

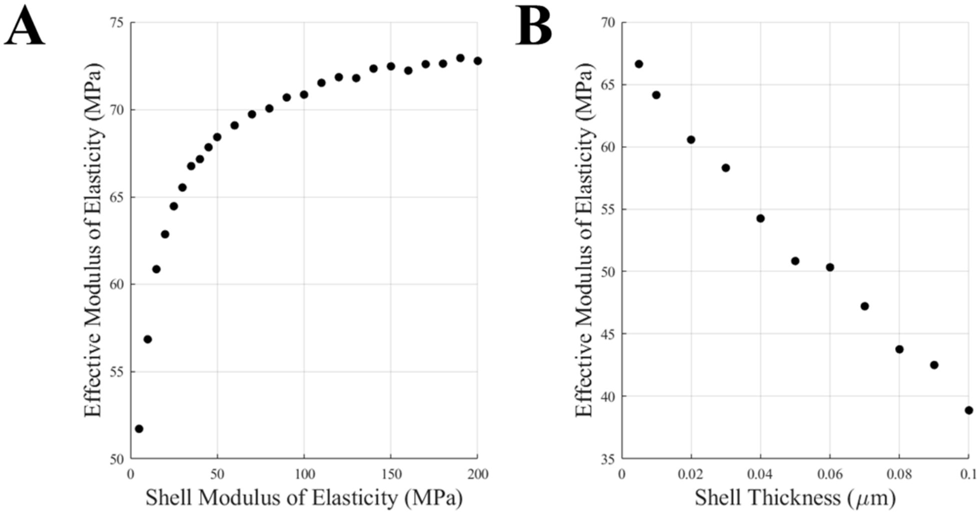

Figure 17: Effect of shell elastic modulus on overall material elastic modulus

The desired output from the microscale model was a representative elastic modulus for a section of the tensile bar with the input area fraction of iron oxide particles. The modulus was estimated with a simulated tensile pull. One side of the square section was fixed axially, while still allowing tangential strain, and the opposite side of the section was pulled in tension with a prescribed displacement. The model was built on the plane stress approximation to allow for out-of-plane strain to prevent artificial stiffening. The reaction force on the fixed edge was extracted from the solution as the only missing piece in calculating the elastic modulus as seen in Equation 2. This elastic modulus was then passed onto the mesoscale model as the next scale in the multi-scale model.

$$E = \frac{\sigma}{\varepsilon} = \frac{\frac{F_{reaction}}{Area}}{\frac{\Delta L_{prescribed}}{L_0}} = \frac{F_{reaction} L_0}{\Delta L_{prescribed} Area} \qquad \textbf{(2)}$$

The main goal of the mesoscale model was to consider the uneven distribution and gradients of the iron oxide dispersion and calculate a representative modulus of elasticity for the stir region in the tensile bar. The model looked at a lower magnification and larger physical scale SEM image of the sample and split the image into sections. Geometrically, the mesoscale model sectioned a 960um x 1250um rectangle into a 4x5 grid of 250um squares where the bottom row had a reduced height of 210um. The area fraction of iron oxide was calculated in each section from the SEM image as illustrated in Figure 18 and input into the microscale model. The resulting elastic modulus from the microscale model was applied to the corresponding section of the mesoscale model. Each section had a unique modulus of elasticity informed by its area fraction of iron oxide and the microscale model. Like the microscale model, the mesoscale model calculated an overall modulus of elasticity using a tensile pull simulation. The final modulus of elasticity output was a comprehensive modulus that was applied to the stirred material region.

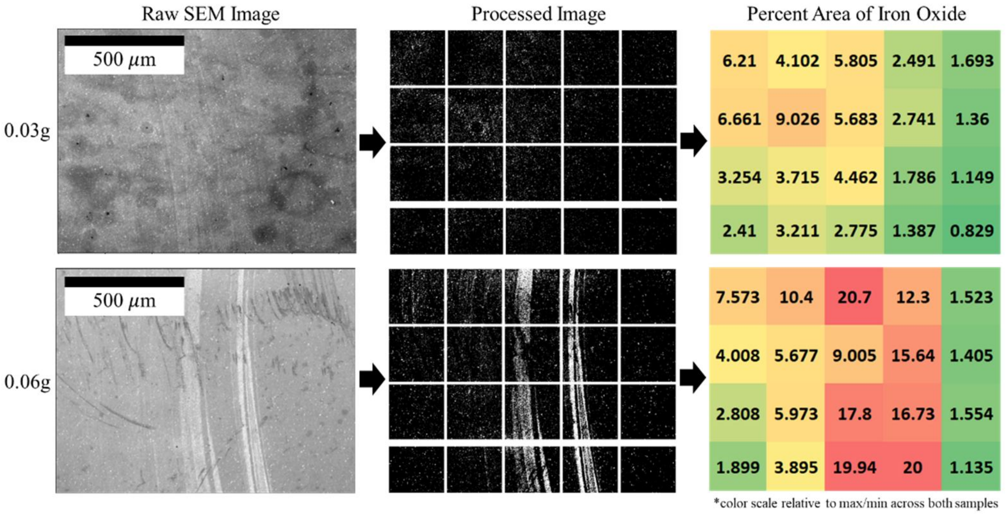

6.21	4.102	5.805	2.491	1.693
6.661	9.026	5.683	2.741	1.36
3.254	3.715	4.462	1.786	1.149
2.41	3.211	2.775	1.387	0.829

7.573	10.4	20.7	12.3	1.523
4.008	5.677	9.005	15.64	1.405
2.808	5.973	17.8	16.73	1.554
1.899	3.895	19.94	20	1.135

Figure 18: Mesoscale area fraction process diagram

The previous two models focused on modeling the composite’s structure to predict material properties based on the aluminum-iron oxide composite structure. The macroscale model used the results from the previous models and solved an eigenvalue problem to estimate the natural frequencies and mode shapes of the tensile bar. The dimensions for the geometry of the tensile bar were kept constant as the average of measurements taken from the samples. Since the tensile bar samples were only stirred with iron oxide in the middle of the gauge section, the tensile bars could not be considered homogeneous and there were two unique materials applied to their geometry. The stir region was assumed to be a cylindrical volume on the center of the tensile bar with a diameter of 30mm where the sides of the stir region were cut away during machining as explained in Section 2.1. The modulus of elasticity calculated in the mesoscale model was applied to the tensile bar stir region. The rest of the tensile bar, mostly made of the grip sections, was given known AA7075 material properties from the given substrate material data. The tensile bar model was built with 3D geometry without symmetry. This made sure all possible natural frequency modes were discovered, as symmetry can hide modes. There were no boundary conditions (BCs) applied to the tensile bar to restrict its motion. This simulated the free boundary condition that LARS aimed to emulate with their experimental setup. Since the model only solved for the natural frequencies, and there were no forces applied, this is an idealized simulation.

Each model run started by calculating the area fraction of iron oxide of each section in the mesoscale grid. Each of these area fractions was input into a microscale model and a unique geometry was generated based on the known size distribution and measured area fraction. The microscale model was then run to estimate the modulus of elasticity of that area. Then the mesoscale model used the microscale results for each section of its grid to estimate the overall modulus of elasticity for the stir region. This final, adapted modulus of elasticity was then input into the stir region of the macroscale tensile bar model for eigenmode analysis.

2.7 Model Results

The first step in testing the model was to attempt to match the LARS-measured frequencies for the 0.0g samples. Since these samples did not contain any iron oxide, the microscale and mesoscale models were not used, and only the macroscale model was used. The elastic modulus applied to the stir region and grip sections was the elastic modulus from the AA7075 T6 material data sheet [29]. The model solved for natural frequency modes between 10 and 40kHz, the same range as LARS measured. As explained in Section 2.2, the model predicts more modes than LARS detects due to the single-direction measurement. However, even after filtering out the modes, LARS would not have been expected to detect, the model still predicted more modes than are seen on the LARS vibration spectrum. So, to account for this discrepancy, the modes in the model closest to the four trackable LARS peaks were extracted from the model. These modes corresponded to out-of-plane bending modes 5-8 as shown in Table 2. The LARS peak values were taken as the average across the 0.0g iron oxide samples. This resulted in a consistent error of less than 2% for the trackable peaks. As illustrated in Figure 19, these predicted frequencies show good visual correlation with the LARS signal.

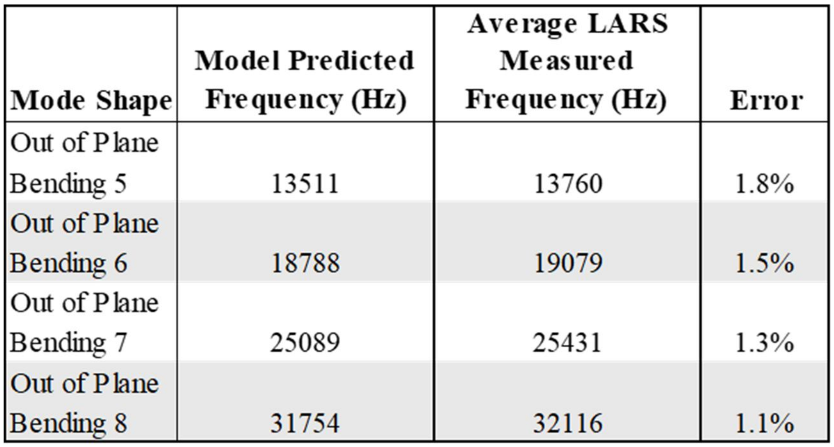

Mode Shape	**Model Predicted Frequency (Hz)**	**Average LARS Measured Frequency (Hz)**	**Error**
Out of Plane Bending 5	13511	13760	1.8%
Out of Plane Bending 6	18788	19079	1.5%
Out of Plane Bending 7	25089	25431	1.3%
Out of Plane Bending 8	31754	32116	1.1%

Table 2: 0.0g Samples' natural frequencies predicted by multi-scale model

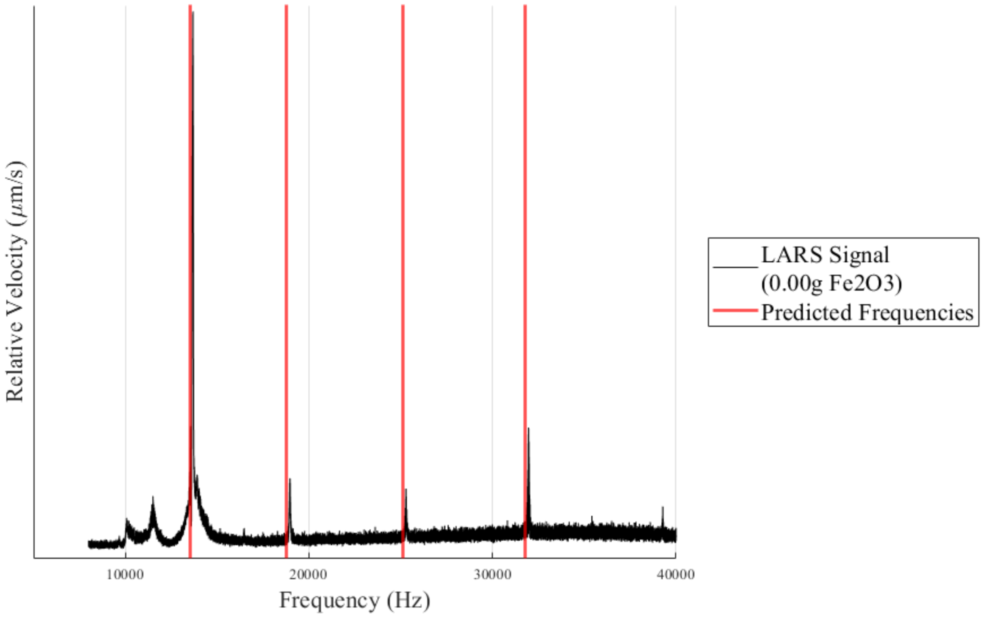

Figure 19: 0.0g multi-scale model predicted frequencies overlayed on LARS vibration spectrum

With the 0.0g iron oxide baseline sample predictions established, the next step in testing the model was to begin looking at the contaminated samples. The models for these samples included the microscale and mesoscale models to predict the modulus of elasticity for the stir region. However, the unknown shell parameters still needed to be tuned. So, the model for these samples ran several times with different values for the shell modulus of elasticity and thickness. From these runs a shell modulus of 10GPa and a thickness of 30nm were chosen. These values were chosen to yield relatively consistent prediction error of 1-2% between the model and LARS when compared to the 0g samples, as shown in Table 3. The same modes were considered for each sample group as well. The results of these sample groups also showed a similar visual correlation as the 0.0g sample group illustrated in Figure 20. The model was able to predict the natural frequencies with an average error of 1.2% between all three sample groups. The combination of all these results demonstrated that the model could predict the natural frequencies of an AFSD part with or without iron oxide contamination with a consistent error to the LARS-measured value.

	0.03g Sample Group			0.06g Sample Group		
Mode Shape	**Model Predicted Frequency (Hz)**	**Average LARS Measured Frequency (Hz)**	**Error**	**Model Predicted Frequency (Hz)**	**Average LARS Measured Frequency (Hz)**	**Error**
Out of Plane Bending 5	13461	13684	1.6%	13339	13469	1.0%
Out of Plane Bending 6	18716	18986	1.4%	18501	18695	1.0%
Out of Plane Bending 7	25004	25301	1.2%	24762	24938	0.7%
Out of Plane Bending 8	31608	31977	1.2%	31338	31530	0.6%

Table 3: Predicted frequencies and error for 0.03g and 0.06g iron oxide sample groups from multi-scale model

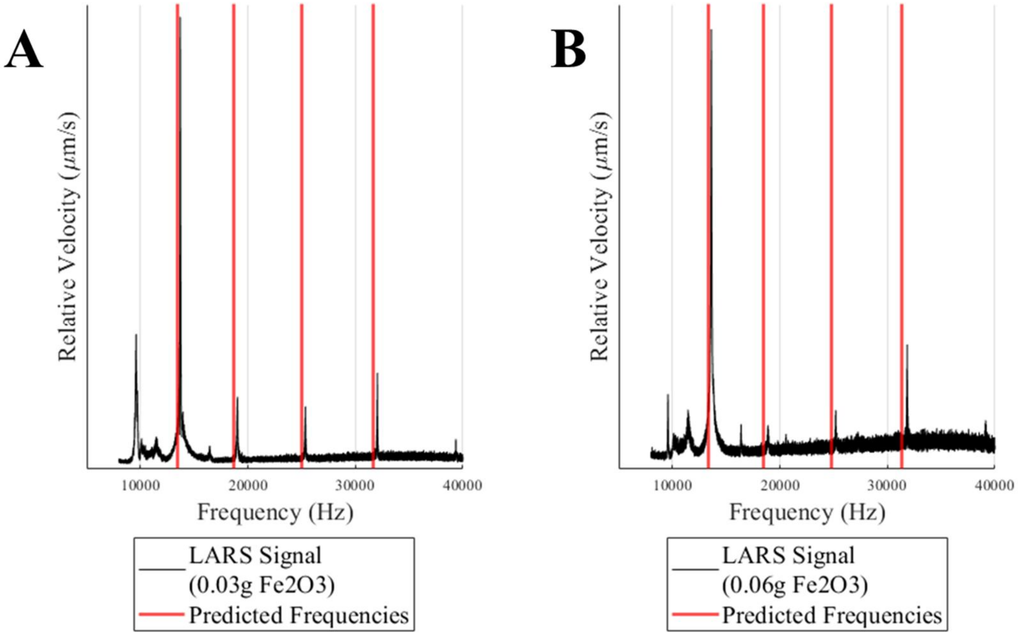

Figure 20: Multi-scale model predicted frequencies overlayed on LARS vibration spectra: (A) 0.03g Sample, (B) 0.06g Sample

With the shell parameters tuned based on the LARS measurement results, the estimated material properties of the stir region could finally be analyzed. As explained in Section 2.2, the elastic modulus of the stir region was hypothesized to decrease with the amount of iron oxide contamination. This hypothesis was applied to the multiscale model by making the stir region elastic modulus variable through estimation. The multiscale model predicted elastic moduli are shown in Figure 21. The model estimated a value of around 69GPa for 0.03g samples and 65GPa for 0.06g samples, which decreased from a raw elastic modulus of 72GPa. Following the model, these values represented a prediction for the elastic moduli of the stir region, assuming it could be considered homogeneous. Although high variation was seen in the tensile testing results, the model-predicted moduli fell within the range of variation seen in testing. This demonstrated that the predicted elastic moduli were well within the range of possible values.

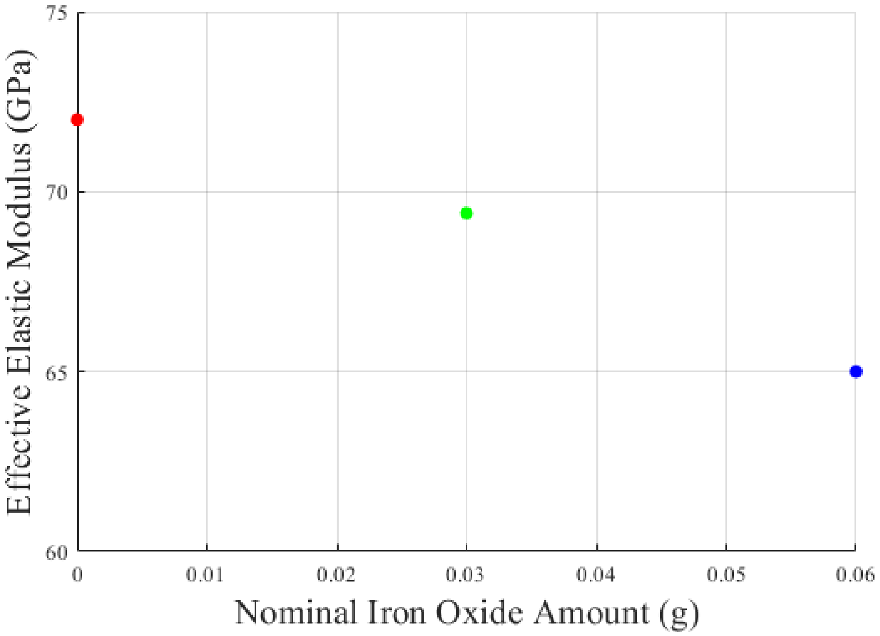

Figure 21: Plot of Estimated Effective Stir Region Elastic Moduli

Chapter 3: Voxel Model

3.1 Printing the Second Batch of Samples

In a continuation of the case study and due to the limited frequency shifts seen in the first batch of samples, a second batch of samples was created with different amounts of iron oxide and more intense flaws. Nine samples were printed for this second batch with three each of 0.04g, 0.12g, and 0.20g of iron oxide powder. A hole repair print was utilized again, see Section 2.1, and printing was conducted on the same AFSD machine for the second sample batch. However, a few print process parameters were changed, which resulted in worse repairs or more intense flaws. Notably, these changes included a reduced stirring time on each layer and one less layer being printed per sample which meant that less stirring occurred in each sample. These changes for the second sample batch led to the formation of voids within some of the samples as shown in Figure 22.

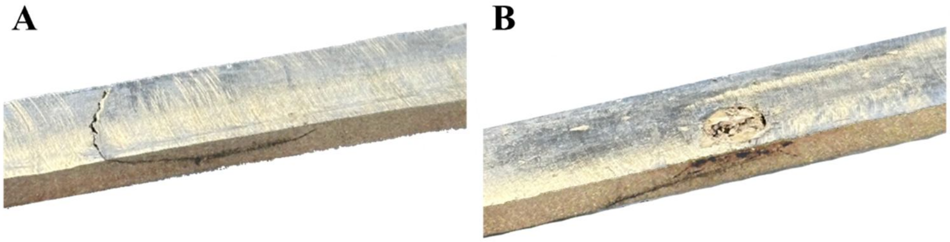

Figure 22: Batch 2 sample with visible voids: (A) Bottom of the sample with a crack running along the face and side, (B) Top of the sample with from stir

The introduction of these voids had a few important implications that needed to be considered throughout the remainder of the case study. First, the presence of voids changed the tensile bar geometry meaning that the samples can no longer be considered solid and homogeneous. Also, the presence of voids created stress concentrations and changes in the cross-section area which had a pronounced effect on tensile testing. The voids also prevent direct comparison between the first and second batch of samples based on iron oxide amount, as their flaws are fundamentally different. The last major consideration is that the voids prevented a direct correlation between initial iron oxide amount and frequency response, as the samples with voids were expected to behave fundamentally differently than samples without.

3.2 Non-Destructive Testing

Like the first batch of samples, the second batch of samples was machined and sent to Metro Laser to have the vibration spectra measured via LARS. The difference with the second batch of samples was a change to use the net setup, discussed in Section 1.3.3, which used a net for part holding rather than a rigid surface. The switch in setups was a developmental upgrade to the LARS setup made by Metro Laser between the scanning of the two sample batches to reduce the impact of part holding on the measured vibration response to better approximate a free boundary condition. An example frequency response plot for one of each of the iron oxide amounts in the second batch is illustrated in Figure 23. The new net setup helped reduce the noise and damping in the vibration measurements and allowed more natural frequencies to be picked up in the 10 to 40kHz scanning range. The introduction of many more peaks made each peak less distinct and made tracking them across the samples more difficult. This is in part due to an inconsistency in the number of detected peaks across the samples. That is, some samples' frequency response displayed more peaks than others. These counts were even inconsistent within iron oxide sample groups, which makes the reason behind the inconsistency unclear.

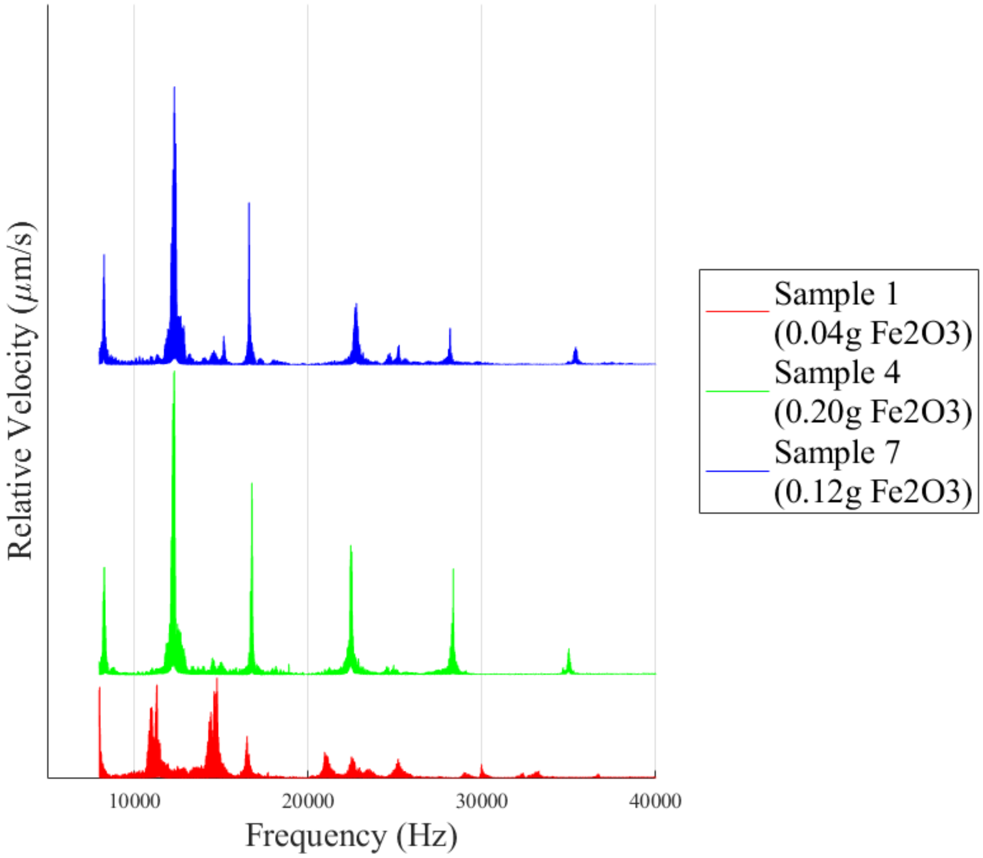

Figure 23: LARS spectrum plots for the second batch of samples

Like the first batch of scans, the natural frequencies were extracted for each sample. However, the sample groups for the second batch of samples did not include a 0.0g baseline, as the changes made to the LARS scanning were only announced after the second batch of samples was produced.

Since the voids took away the solid, homogeneous stir assumption made in modeling the first batch of samples, a new NDT technique was needed that could inform a model about the geometry of the voids and cracks. XCT was an attractive solution to this problem as it gave 3D scanning results which provided an extra dimension of spatial information compared to 2D from

SEM in the first batch. After LARS was performed, the samples were shipped to ZEISS (Wixom, MI) and XCT was conducted using a ZEISS XRadia Versa 620 with a flat panel detector, an 80kVP acceleration voltage, and 3,001 images per 360-degree rotation. The scans encompassed a 29mm x1.9mm x 5.6mm region centered on each tensile bar to maximize the resolution where the stir was conducted. The scans were post-processed by ZEISS to highlight regions of different densities within the samples. Knowing that iron oxide has a density of nearly double AA7075, areas of low density were assumed to be voids, and areas of higher density were assumed to contain iron oxide, as iron oxide is assumed to be the only possible contaminant. An example XCT scan is illustrated with a 3D model of the scan in Figure 24.

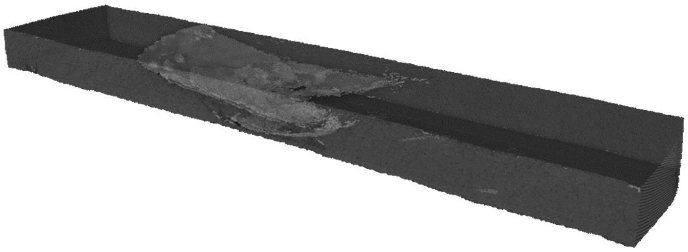

Figure 24: XCT scan results example

Assuming each sample consists of base AA7075, contaminated regions with iron oxide, and voids; the samples can be treated as a ternary system with these three regions. This allows for the simplification of the raw 2D XCT images into such a ternary system with 3 distinct colors as illustrated in Figure 25. A Scharr operator was applied to the raw grayscale XCT images to detect boundaries for the ternary system. One of the three colors was then applied to each boundary within the images. The result was an image with only three distinct colors. However, further details about the image processing procedure were outside of the scope of this work.

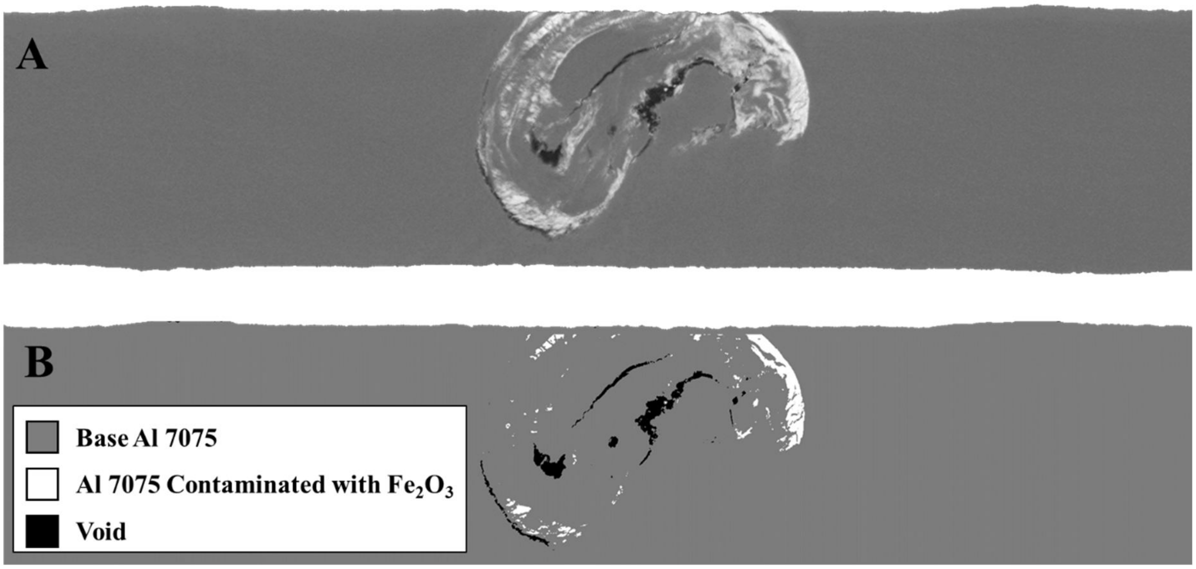

Figure 25: (A) Raw XCT image, (B) Processed ternary image

3.3 Voxel Model Overview and Mesh Processing

The multi-scale model discussed in Chapter 2 only considers the effect of iron oxide particles mixed into an AA7075 matrix. With processed XCT images and the introduction of voids with the second batch of samples, a second model was built for eigenmode analysis, as the multi-scale model discussed in Chapter 2 could not consider the effect of voids and its underlying assumptions could no longer be made for the new batch of samples. The new model is based on using XCT data to build a 3D mesh for simulation. The new model will consist of three material regions for the grip sections, the stir region, and the iron oxide contaminated regions accordingly. Although it was possible to create a 3D model directly from the XCT scans and feasible to create a dual material mesh from this model for FEA, this is an impractical approach. The high resolution of the XCT scans resulted in a high-resolution 3D solid body that was computationally expensive and time-consuming to process before even considering building an FEA model from it. The natural solution to this problem was to reduce the resolution of the direct 3D solid body and its mesh. However, doing so resulted in feature loss and smoothing that made generating a multi-material mesh very difficult and relatively inaccurate. Also, the use of an arbitrary geometry in this way would require the use of tetrahedral elements for meshing, which as explained in Section 1.4.1, is not ideal. So, a meshing process was developed that leverages the XCT images without directly using an XCT solid body.

This process is centered around modifying an existing tensile bar mesh to carve out the voids and change the material of elements in areas that contain iron oxide. A 2D process diagram of this procedure is shown in Figure 26. The meshing process began with a solid, homogeneous 3D model of the tensile bar geometry. The model was partitioned into two sections: the grips and the XCT scan volume. This partition sped up the mesh processing, as the grip regions outside of the XCT scan area were left untouched, and the mesh processor only needed to consider the elements within the scan region. The tensile bar model was then meshed with hexahedral elements, the size of which was directly controllable. This resulted in a solid mesh of a single material which could be processed using XCT image data. The XCT images were probed in a grid, based on the mesh size, to check which of the three possible ternary components was at each point. If the component was void or iron oxide, the point's XYZ coordinates and component type (void or iron oxide) were recorded to a list. A list of points was generated from the stack of XCT images for each sample. Each sample's list of contaminant and void points and the homogeneous mesh were fed into the mesh processor. The processor matched the points to elements for material change or deletion, conducted the change and deletion, and then rebuilt the mesh so it could be read by the FEA program. The processed meshes were then imported into the FEA program and the grip meshes were reattached to each to create a full tensile bar model of each sample as illustrated in Figure 27.

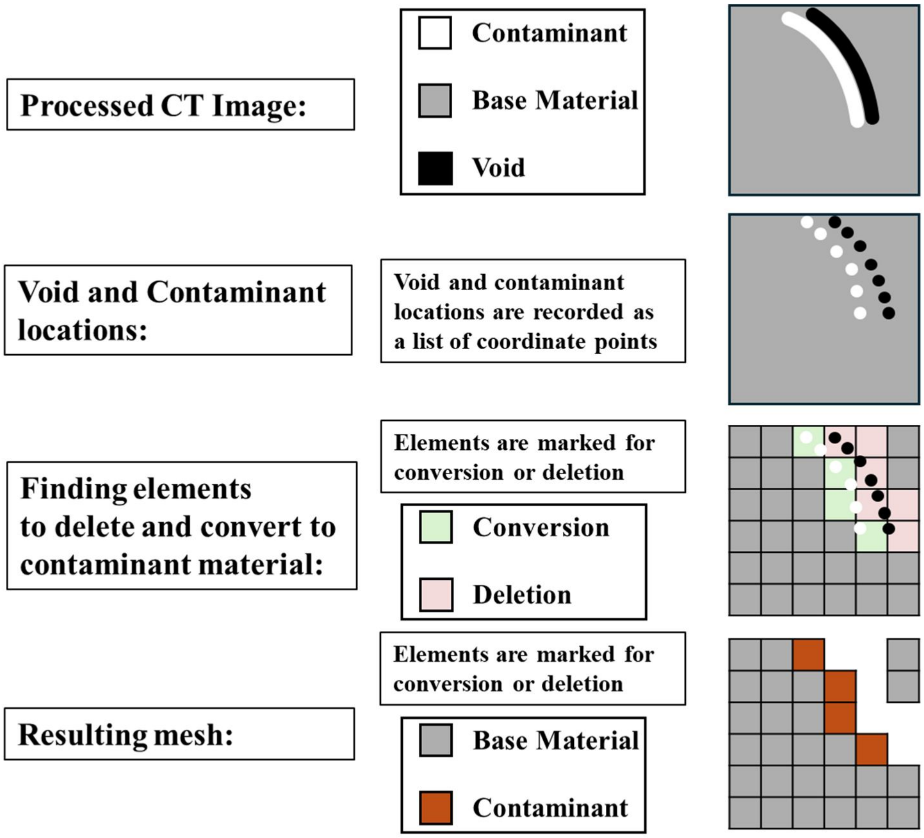

Figure 26: 2D Void mesh processing diagram

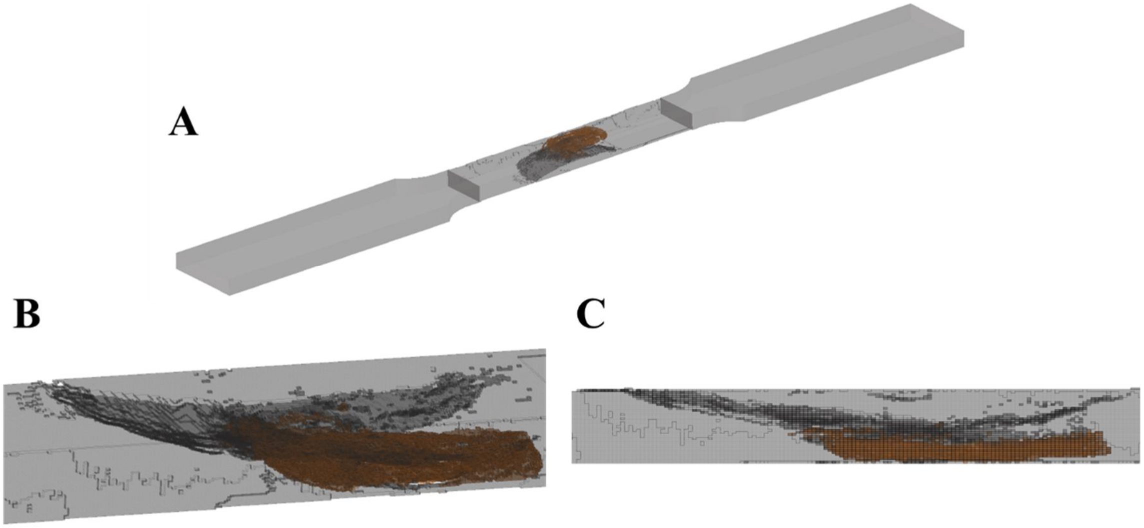

Figure 27: Full tensile bar processed mesh images: (A) Full Tensile Bar View, (B) Closeup of void and contaminant regions, (C) Side view of void and contaminant

Some of the XCT scans included rounded edges at the far ends of the scan due to the scanning boundaries. Through the ternary image processing, these edges added extra void locations to the list of void points. This resulted in artificial cracks and voids in processed meshes as illustrated in Figure 28. So, on samples that had these rounding artifacts, the void boundaries were cropped to remove these artifacts.

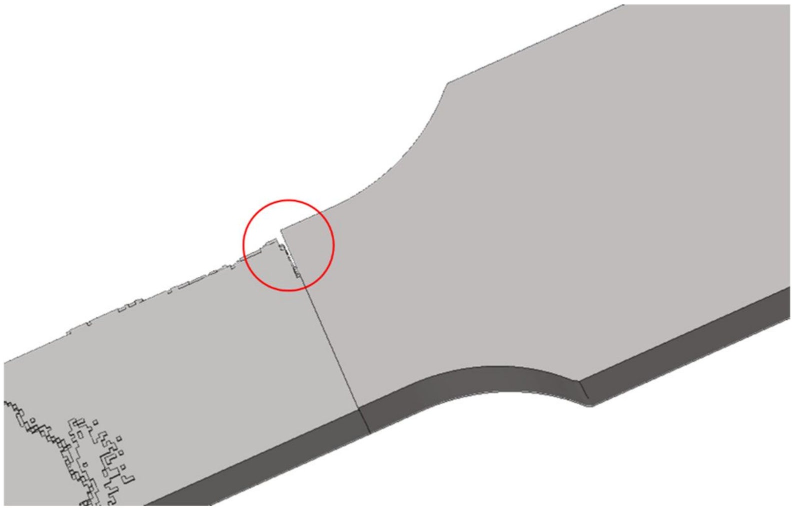

Figure 28: Artificial crack in processed mesh due to XCT scan boundary

3.4 Model Results

The material properties of the grip sections were given properties from the AA7075 T6 material data sheet [29]. The aluminum in the center stir region was given the same density as the grip sections and an elastic modulus of 65GPa as the average of the first sample batch's average tensile pull. However, the material properties of the contaminated regions of iron oxide were unknown and needed to be tuned. To explore these tunings of the material properties of iron oxide, the bounds of reasonable material property values were used to get a sense of how the model results compared to the LARS spectrum. These bounds included a very low elastic modulus based on the assumption that the iron oxide was not well mixed with the aluminum which left clumps of loose powder in the tensile bars. The high end of the bounds was double to modulus of the wrought AA7075 or about 144GPa. After running the model with various elastic moduli applied to the contaminated regions, a low elastic modulus of 1GPa was found to yield the lowest error in correlating the model predictions to LARS frequency peaks.

The model was run for each of the samples in the second batch and the predicted frequency modes were compared to the peaks extracted from the LARS data. An example from each iron oxide group is shown in Table 4. The average error from the voxel model in predicting the LARS measured value fell into the same range as the multi-scale model's error. However, there were a few modes that had considerably high error (>5%) compared to the rest. There were also a few modes that the model predicted that LARS did not pick up in all the samples. There were also LARS peaks excluded from this table that the model did not have a corresponding frequency. These discrepancies became evident when plotting the predicted frequencies over the LARS spectra, as shown in Figure 29.

	Sample 1 (0.04g)			**Sample 4 (0.12g)**			**Sample 8 (0.20g)**		
Mode Shape	**LARS Frequency (Hz)**	**Model Frequency (Hz)**	**Error**	**LARS Frequency (Hz)**	**Model Frequency (Hz)**	**Error**	**LARS Frequency (Hz)**	**Model Frequency (Hz)**	**Error**
Out of Plane Bending 5	11312	11694	3.4%	12234	12146	0.7%	12234	12028	1.7%
Twisting 2	15312	15411	0.6%	15155	15262	0.7%	-	15540	-
Out of Plane Bending 6	16763	16515	1.5%	16606	16827	1.3%	16430	16820	2.4%
Twisting 3	17704	18151	2.5%	18057	18658	3.3%	18234	18527	1.6%
Out of Plane Bending 7	22508	21793	3.2%	22704	22238	2.1%	-	22272	-
Twisting 4	24998	25135	0.5%	24704	24483	0.9%	24626	24811	0.8%
Out of Plane Bending 8	28979	28013	3.3%	28175	28737	2.0%	26704	28396	6.3%
Out of Plane Bending 9	33214	33755	1.6%	-	34788	-	30998	34871	12.5%
Twisting 5	32371	33133	2.4%	35390	35131	0.7%	-	35231	-
Twisting 6	36665	39158	6.8%	41037	38835	5.4%	38273	38757	1.3%
		Average Error:	2.6%		**Average Error:**	1.9%		**Average Error:**	3.8%

Table 4: Voxel model predicted frequencies compared to LARS-measured frequencies

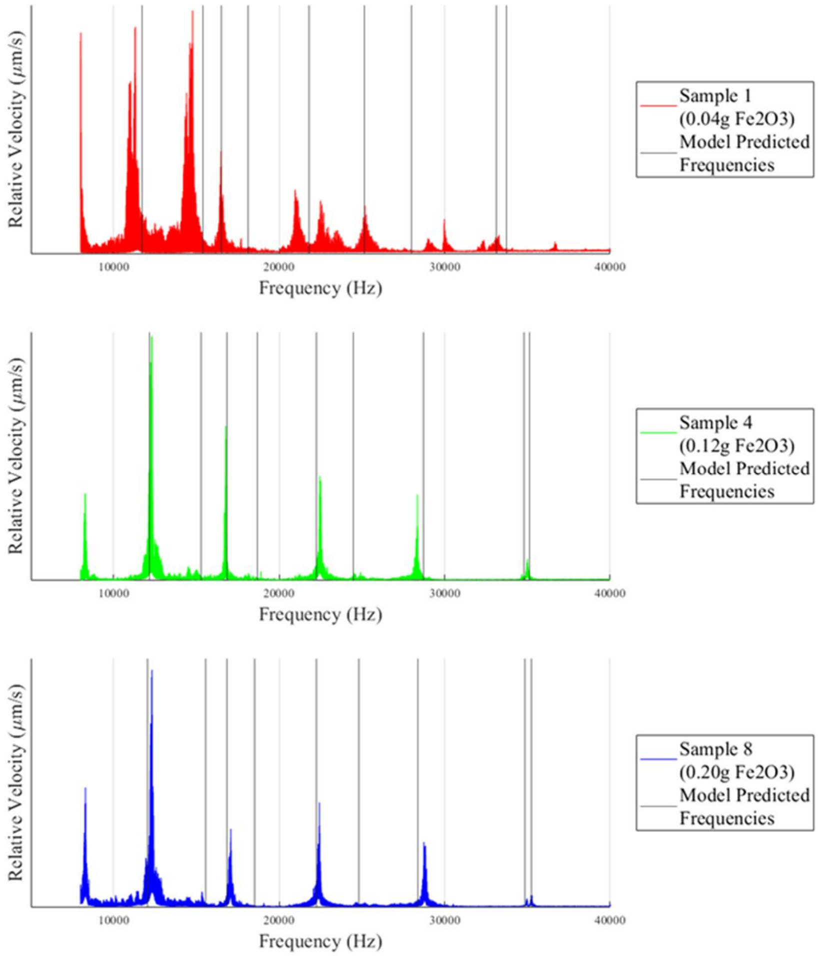

Figure 29: Voxel model frequency predictions overlayed on LARS frequency spectra

Chapter 4: Conclusions, Future Work, and References

4.1 Modeling Path Forward

Both models have shown their ability to predict the natural frequencies of the AFSD tensile bar specimens, as both exhibit a relatively low average error in their predictions. There are a few paths forward for further modeling with this project. The first of which is transient frequency simulation. As explained in Section 1.3.2, LARS sweeps through vibration frequencies. This sweeping means that the vibration does not occur at a steady state. LARS also applies vibration through a single actuator rather than whole-part vibrations. A transient simulation could consider these effects to model the LARS setup rather more directly than modeling with an idealized frequency analysis. Another modeling path that could be explored is including boundary conditions other than a free boundary, as was used for both the models discussed in this paper. Although the LARS setups used for data collection in this work aimed to approximate a free boundary condition, part holding in any form will influence the frequency response as is evident from the change in part holding from the first to the second batch of samples in this work. These boundary conditions could include rigid contact surfaces, friction, or damping on some of the part faces. In the same modeling direction, a rigid boundary condition could also be explored. If the part was held rigidly or with other well-defined boundary conditions, these could be translated into a model. For example, with the tensile bar specimens discussed here, setting the tensile bar up as a cantilevered beam would allow for vibration while creating a boundary condition that is easily defined in a modeling environment. The last recommendation for future work on modeling is fracture modeling of the second samples with cracks and voids. The multiscale model was able to predict the elastic moduli in the stir region through the iron oxide contamination distribution seen in SEM images. The voxel model could be expanded in a similar manner to predict the elastic moduli and failure modes of the void containing specimens. This additional modeling would give insight into the material behavior for these more complex samples under a mechanical load.

4.2 Proposed New Experimental Setup for LARS

To improve how LARS data can be used in conjunction with modeling, the LARS setup needs to be better understood based on how its measurement is related to and affects the part’s frequency response. The first component of the experimental setup that is not conducive to modeling is the part-holding apparatus. Well-defined boundary conditions, even if they were more constrictive to the part, would make for better modeling assumptions. A rendering of what this setup could look like is illustrated in Figure 30. To prevent the influence of the setup on the measured frequency spectrum, the part and piezo mounts both need to be considered rigid. For this proposed setup, the piezo mount and part mount are made from relatively large blocks of steel that are bolted to the measurement surface. This surface should also be rigid. A cantilever setup works well for the tensile bar as it is a long, slender geometry. However, this setup will not necessarily work for arbitrary geometry and different part holding could be necessary. The second of these is the piezoelectric actuator. The piezo physically contacts the part for excitation which could lead to dampening or affect the frequencies of the part. The piezo is also mounted on a relatively long rod, and this arm could see vibrations that are being read into the signal. Improvements could be made to this part of the setup by reducing the standoff length of the piezo from the rod, increasing the stiffness of the mount, or using a non-contact excitation device that uses sonic or ultra-sonic frequencies to induce vibrations.

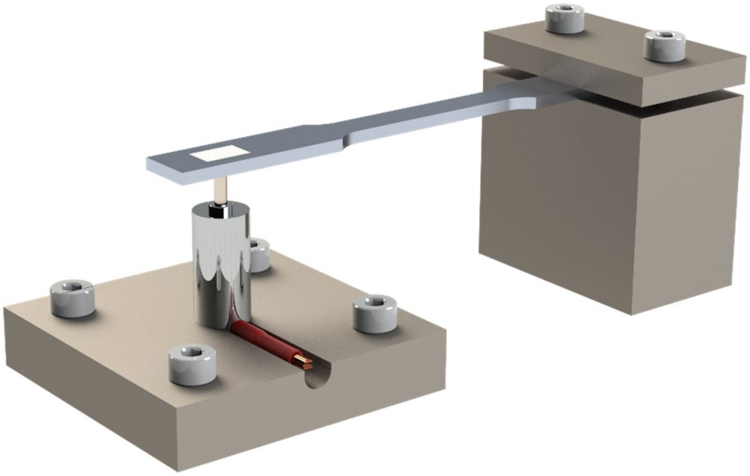

Figure 30: Conceptual cantilever LARS setup render

4.3 In-Situ Monitoring

As an ongoing study, this project ultimately aims for an in-situ monitoring solution using LARS. This case study only aimed to serve as a proof of concept for the LARS vibration measurement system as an NDT system in conjunction with modeling to detect peak shifts of a part due to a print flaw. The next step in this process should not be a leap to full in-situ detection. A median experiment should be conducted that simply involves mid-print inspection using the LARS system. However, for the sake of repeatability, it is undesirable to remove the substrate mid-print, as this will introduce variation into the print geometry, which affects the modal response. But this creates an issue when considering that a print substrate should be relatively fixed, as this does not allow for deformation into vibration modes for LARS measurement. This dilemma leaves two categories of future experimental setups: larger-scale prints that can deform and vibrate with a fixed substrate or a substrate mount with transformable boundary conditions.

An experimental setup conceptual design is illustrated in Figure 31 that allows the substrate to remain bolted to a backing structure with a secondary supporting plate that can be removed between print layers to leave most of the substrate unsupported in a near-cantilevered configuration for LARS measurement. The secondary support plate also includes cam clamps that help to fix the substrate in place. These are preferable compared to additional bolts, as the cam clamps simply need to be loosed for removal and provide tolerances for reinstallation of the support plate. The main backing piece that the substrate is bolted to also includes a cutout near the far overhanging end of the substrate. This cutout provides space for the piezo actuator to slide in underneath the substrate for excitation and measurement. The piezo actuator is mounted to an assembly with a locking screw mechanism that allows for precise height adjustment. The piezo mount will register against dowel pins and bolt into place onto the machine's bed for repeatable measurements, as it needs to be removed between print layers to make space for the supporting plate.

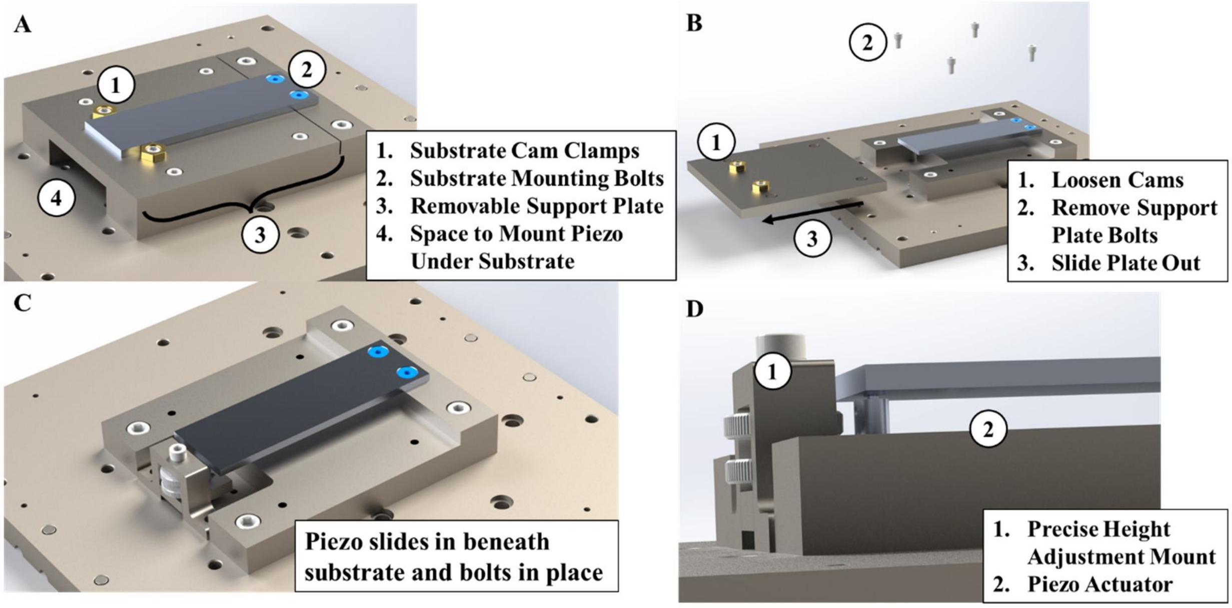

Figure 31: Mid-print analysis, cantilevered experimental setup concept: (A) Print setup overview, (B) Transformation to cantilevered measurement setup, (C) Cantilevered top view, (D) Piezo placement closeup

This setup also supports filling the gap between LARS and modeling by defining clearer boundary conditions. For example, the section of the bottom face of the substrate that contacts the backing structure could be set as a fixed boundary condition. This is the simplest boundary condition assumption. If this is not sufficient, then the bolt holes could be fixed, and the back surface could be modeled as a contact surface with the support structure.

Considering another step into the future, a final, automated version of LARS in situ with AFSD could look something like what is illustrated in Figure 32. Here, the setup focuses on eliminating the need for human or operator interaction with the machine while printing and monitoring for defects. Therefore, this setup considers the case where the substrate stays in place and full-scale parts are measured directly without unclamping. The piezo is mounted to a robotic arm in this setup, as this allows excitation in multiple positions on a part and allows printing of arbitrary geometry. Working towards a LARS in situ contamination detecting setup, like the one proposed here, requires a better understanding of the LARS measurement, boundary conditions, and defects expected in the printing environment.

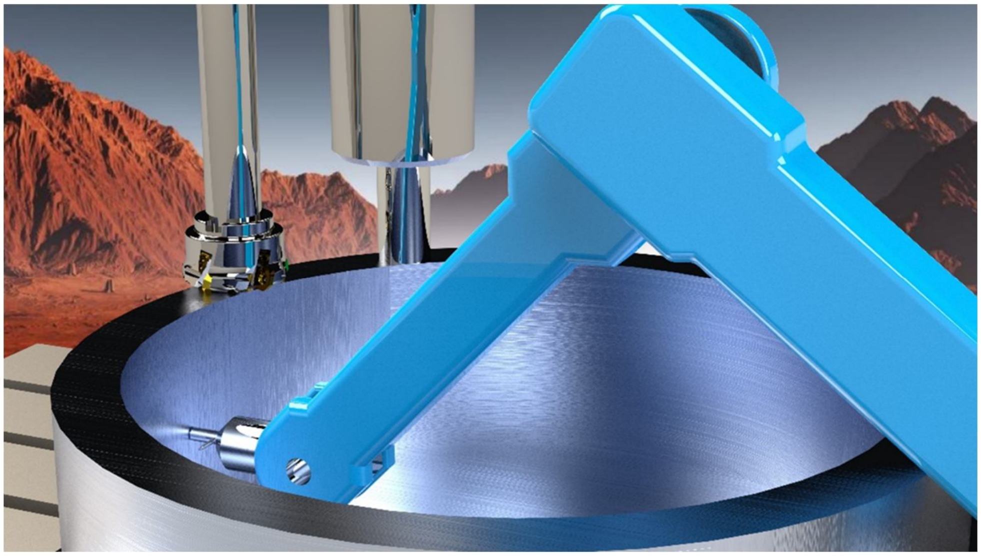

Figure 32: Fully automated LARS in-situ concept render

With arbitrary geometry (measuring a printed part in situ at a random layer height), determining the actual change in the material properties becomes ambiguous without knowledge of the defect and its location. For these experiments, the defect location, size, and cause were known, and the only unknown was the amount of iron oxide that contaminated the print. Assuming the resonance monitoring takes place between layers, the location, size, quantity, and cause of the potential defects would be unknown. That is, the defect(s) could be located at any point within the last printed layer and caused by various sources of error. Depending on the geometry of the printed part, it is feasible to pinpoint the location of the defect using known node and peak locations. When a defect lies on a natural frequency node, the defect will have a lesser impact on the frequency than when it lies on a peak. So, by stimulating various points creating different sets of nodes, or simply determining which frequencies shifted, it is conceivable to determine the defect location through the overlap of these node and peak displacement points. If some frequencies shift and a particular frequency does not shift, the defect should lie on one of that frequency's nodes. Or if the frequency shifts a lot, the defect should lie on a peak deformation location for that natural frequency.

4.4 References

[1] J. Boyer, C. Seepersad, T. W. Simpson, C. B. Williams, and P. Witherell, “Special Section: Designing for additive manufacturing recent advances in design for additive manufacturing,” *Journal of Mechanical Design*, vol. 139, no. 10, pp. 100901–100902, Oct. 2017, doi: 10.1115/1.4037555/366997.

[2] R. Chen, F. Imani, E. Reutzel, and H. Yang, “From Design Complexity to Build Quality in Additive Manufacturing-A Sensor-Based Perspective,” *IEEE Sens Lett*, vol. 3, no. 1, Jan. 2019, doi: 10.1109/LSENS.2018.2880747.

[3] M. Javaid, A. Haleem, R. P. Singh, R. Suman, and S. Rab, “Role of additive manufacturing applications towards environmental sustainability,” *Advanced Industrial and Engineering Polymer Research*, vol. 4, no. 4, pp. 312–322, Oct. 2021, doi: 10.1016/J.AIEPR.2021.07.005.

[4] S. Ford and M. Despeisse, “Additive manufacturing and sustainability: an exploratory study of the advantages and challenges,” *J Clean Prod*, vol. 137, pp. 1573–1587, Nov. 2016, doi: 10.1016/J.JCLEPRO.2016.04.150.

[5] N. Knofius, M. C. van der Heijden, and W. H. M. Zijm, “Moving to additive manufacturing for spare parts supply,” *Comput Ind*, vol. 113, p. 103134, Dec. 2019, doi: 10.1016/J.COMPIND.2019.103134.

[6] N. Sanaei, A. Fatemi, and N. Phan, “Defect characteristics and analysis of their variability in metal L-PBF additive manufacturing,” *Mater Des*, vol. 182, p. 108091, Nov. 2019, doi: 10.1016/J.MATDES.2019.108091.

[7] I. Gibson, D. Rosen, B. Stucker, and M. Khorasani, *Additive Manufacturing Technologies*, Third. Cham, Switzerland: Springer, 2021.

[8] B. K. Panigrahi, “Processing of low carbon steel plate and hot strip-an overview,” *Bulletin of Materials Science*, vol. 24, no. 4, pp. 361–371, 2001, doi: 10.1007/BF02708632/METRICS.

[9] S. J. Qin, “Survey on data-driven industrial process monitoring and diagnosis,” *Annu Rev Control*, vol. 36, no. 2, pp. 220–234, Dec. 2012, doi: 10.1016/J.ARCONTROL.2012.09.004.

[10] S. K. Everton, M. Hirsch, P. I. Stavroulakis, R. K. Leach, and A. T. Clare, “Review of in-situ process monitoring and in-situ metrology for metal additive manufacturing,” *Mater Des*, vol. 95, pp. 431–445, Apr. 2016, doi: 10.1016/J.MATDES.2016.01.099.

[11] Y. AbouelNour and N. Gupta, “In-situ monitoring of sub-surface and internal defects in additive manufacturing: A review,” *Mater Des*, vol. 222, p. 111063, Oct. 2022, doi: 10.1016/J.MATDES.2022.111063.

[12] D. Garcia *et al.*, “In situ investigation into temperature evolution and heat generation during additive friction stir deposition: A comparative study of Cu and Al-Mg-Si,” *Addit Manuf*, vol. 34, Aug. 2020, doi: 10.1016/j.addma.2020.101386.

[13] H. Z. Yu *et al.*, “Non-beam-based metal additive manufacturing enabled by additive friction stir deposition,” *Scr Mater*, vol. 153, pp. 122–130, Aug. 2018, doi: 10.1016/j.scriptamat.2018.03.025.

[14] R. S. Mishra, R. S. Haridas, and P. Agrawal, “Friction stir-based additive manufacturing,” *Science and Technology of Welding and Joining*, vol. 27, no. 3. Taylor and Francis Ltd., pp. 141–165, 2022. doi: 10.1080/13621718.2022.2027663.

[15] J. K. Yoder, R. J. Griffiths, and H. Z. Yu, “Deformation-based additive manufacturing of 7075 aluminum with wrought-like mechanical properties,” *Mater Des*, vol. 198, Jan. 2021, doi: 10.1016/j.matdes.2020.109288.

[16] R. J. Griffiths *et al.*, “A Perspective on Solid-State Additive Manufacturing of Aluminum Matrix Composites Using MELD,” *J Mater Eng Perform*, vol. 28, no. 2, pp. 648–656, Feb. 2019, doi: 10.1007/s11665-018-3649-3.

[17] R. Joey Griffiths, D. T. Petersen, D. Garcia, and H. Z. Yu, “Additive friction stir-enabled solid-state additive manufacturing for the repair of 7075 aluminum alloy,” *Applied Sciences (Switzerland)*, vol. 9, no. 17, Sep. 2019, doi: 10.3390/app9173486.

[18] L. P. Martin, A. Luccitti, and M. Walluk, “Repair of aluminum 6061 plate by additive friction stir deposition,” *International Journal of Advanced Manufacturing Technology*, vol. 118, no. 3–4, pp. 759–773, Jan. 2022, doi: 10.1007/S00170-021-07953-Z/FIGURES/14.

[19] G. G. Stubblefield *et al.*, “Ballistic Evaluation of Aluminum Alloy (AA) 7075 Plate Repaired by Additive Friction Stir Deposition Using AA7075 Feedstock,” *Journal of Dynamic Behavior of Materials*, vol. 9, no. 1, pp. 79–89, Mar. 2023, doi: 10.1007/S40870-022-00363-6/FIGURES/8.

[20] “What is Natural Frequency? | SimWiki | SimScale.” Accessed: Mar. 25, 2024. [Online]. Available: https://www.simscale.com/docs/simwiki/fea-finite-element-analysis/what-is-natural-frequency/

[21] “Modal analysis: Theory.” Accessed: Mar. 25, 2024. [Online]. Available: https://www.orcina.com/webhelp/OrcaFlex/Content/html/Modalanalysis,Theory.htm

[22] A. K. Lal, A. K. Dioumaev, D. Dimas, and J. D. Trolinger, “Defect detection in additive manufactured products with a new photonics procedure: a case study,” SPIE-Intl Soc Optical Eng, Jul. 2021, p. 17. doi: 10.1117/12.2594993.

[23] J. D. Trolinger, A. Lal, A. Dioumaev, and D. Dimas, “A non-destructive evaluation system for additive manufacturing based on acoustic signature analysis with laser Doppler vibrometry,” SPIE-Intl Soc Optical Eng, Aug. 2018, p. 12. doi: 10.1117/12.2320445.

[24] D. Dimas, A. Lal, A. K. Dioumaev, and J. Trolinger, "Non-destructive evaluation of additively manufactured metal (AlSi10Mg) brackets using laser Doppler vibrometry and acoustical resonance spectroscopy," SPIE-Intl Soc Optical Eng, Apr. 2020, p. 42. doi: 10.1117/12.2558179.

[25] J. D. Trolinger, J. Gao, C. F. Hess, and A. K. Lal, "A new optical diagnostics tools for grading additive manufactured parts," SPIE-Intl Soc Optical Eng, Sep. 2022, p. 18. doi: 10.1117/12.2633560.

[26] G. P. Nikishkov, "Introduction to the Finite Element Method".

[27] "Eigenfrequency Analysis." Accessed: Mar. 25, 2024. [Online]. Available: https://www.comsol.com/multiphysics/eigenfrequency-analysis

[28] "Composites." Accessed: Mar. 25, 2024. [Online]. Available: https://www.princeton.edu/~humcomp/bikes/design/desi_30.htm

[29] "ASM Material Data Sheet." Accessed: Mar. 30, 2024. [Online]. Available: https://asm.matweb.com/search/SpecificMaterial.asp?bassnum=ma7075t6